Journal of Computational Physics 564 (2026) 115151

Contents lists available at ScienceDirect

Journal of Computational Physics

journal homepage: www.elsevier.com/locate/jcp

Geometry reconstruction from magnetic resonance velocimetry measurements via solving an inverse fluid flow problem

Shota Ito [a,b,*], Alexander Zimmermann [c], Julius Jeßberger [a,d], Stephan Simonis [a,d], Adrian Kummerländer [a,d], Fedor Bukreev [a,b], Jorg Thöming [c], Georg Pesch [e], Mathias J. Krause [a,b,d]

[a] Lattice Boltzmann Research Group, Karlsruhe Institute of Technology, Karlsruhe, Germany
[b] Institute of Mechanical Process Engineering and Mechanics, Karlsruhe Institute of Technology, Karlsruhe, Germany
[c] Center for Environmental Research and Sustainable Technology, University of Bremen, Bremen, Germany
[d] Institute for Applied and Numerical Mathematics, Karlsruhe Institute of Technology, Karlsruhe, Germany
[e] School of Chemical and Bioprocess Engineering, University College Dublin, Dublin, Ireland

ARTICLE INFO

Keywords:
Topology optimization
Computational fluid dynamics
Lattice Boltzmann methods
Gradient-based optimization
Inverse problem
Magnetic resonance velocimetry
Computer tomography scans

ABSTRACT

Computational fluid dynamics (CFD) simulations are an essential method for addressing complex physical flow problems, e.g., heterogeneous reactive flows through open cell foams (OCF) with catalytic coating. To conduct numerical studies in such intricate flow domains, expensive methods such as computer tomography (CT) scans might be necessary to acquire the morphological model. The current work explores an alternative approach to obtain the flow domain from given or measured velocity distributions, where the latter are acquired through magnetic resonance velocimetry (MRV). An inverse Navier–Stokes problem is solved by a numerical framework implemented in the open source library OpenLB, combining the adjoint homogenized lattice Boltzmann method and the quasi-Newton method LBFGS. Therein, the deviation between the measured and simulated velocity distributions is the target of the minimization problem by iteratively adjusting the permeability distribution in the flow, representing the reconstructed topology model. Comprehensive numerical experiments investigate the impact of different aspects, e.g., numerical grid resolution, Reynolds number, and amplitude of artificial noise signals on the input velocity data, on the inverse problem. First, simulated velocity distributions using a CT-scan model of the OCF and then measured MRV data are used as the input for the inverse problem. In the latter, the reconstructed topology is compared against the CT-scan model. We demonstrated that a complex geometry such as the OCF can be reconstructed from velocity distributions (Jaccard index of 0.91) and identified optimal parameter regimes for the framework to operate. Finally, for the case where measured input data were used we archived an improvement of 12% regarding the recovered geometry over the geometry obtained from the signal amplitude image from magnetic resonance imaging.

1. Introduction

Heterogeneous catalysis takes part on 90% of all industrial chemical processes that their performance directly impacts economic and ecological sustainability [1]. Efficient heterogeneous catalysts can enhance reaction rates, reduce energy consumption, and

* Corresponding author.
E-mail address: shota.ito@kit.edu (S. Ito).

https://doi.org/10.1016/j.jcp.2026.115151
Received 18 June 2025; Received in revised form 29 May 2026; Accepted 18 June 2026
Available online 22 June 2026
0021-9991/© 2026 The Author(s). Published by Elsevier Inc. This is an open access article under the CC BY-NC-ND license (http://creativecommons.org/licenses/by-nc-nd/4.0/).

minimize waste, leading to more environmentally friendly industrial processes and lower costs. The open-cell foam (OCF) has beneficial properties for catalysis such as their high radial mixing properties and large surface area where a catalytic porous wash-coat layer enables the reactants to adsorb for reaction [2–4].

Numerous computational fluid dynamics (CFD) studies are conducted for the OCF addressing the pressure loss [4,5], heat transfer problems [6–8], and heterogeneous catalysis [9–12]. There are several approaches to obtain a geometry model for the flow domain in numerical simulations. Parameterized shape models like Kelvin cells or models based on various tessellation techniques provide flexible geometry descriptions regarding morphological parameters such as porosity [10,13]. Commonly, the parameterized models describe only a representative elementary volume (REV) element, and periodic boundaries expand the domain to match the dimensions of the entire foam. This technique has the advantage of reducing computational cost and not to lose the generality of the obtained results, when contrarily a real specific foam geometry is used [10,13–16]. However, as a consequence, homogeneous properties are assumed for the REV, whereas other numerical studies conducting simulations using the whole OCF geometry claim the homogeneity assumption to be not always feasible [8,17]. The OCF geometry required in full-field studies is usually obtained via μ-computer tomography (CT) scans where it captures two-dimensional image stacks of the structure in a non-destructive and non-invasive way [13,17]. Computer-assisted design (CAD) software process the image stacks to create the necessary surface models for CFD simulations [17,18]. An alternative approach to obtain geometry models presents Magnetic resonance imaging (MRI), but CT-scan-based models are currently the most popular approach due to their superior quality. Creating a surface model from CT-scan images or using MRI still involves a highly manual procedure [19].

Through recent advancements in MRI, it is possible to measure various flow properties such as velocity, temperature, and concentration distributions and presents an established method for validating numerical results with MRI [17,20–26]. A clear advantage of MRI is the ability to allow more detailed comparison of the measured distributions as both CFD and MRI yield 3D spatially resolved distributions instead of integral or local data as it is commonly the case in experimental studies [27,28]. However, the main drawback of MRI is the limited resolution of the field of view and relatively low signal-to-noise-ratio (SNR) [29]. Another more technical challenge poses the alignment of CFD and MRI results regarding the translational and rotational displacement, where in other studies sophisticated techniques are proposed to tackle this problem [17,21,22]. Therefore, an extensive numerical study often involves the combination of CT to obtain a geometry model, especially for complex shapes such as OCF and MRI measurements, for in-depth spatially resolved validation of the computed numerical results. The whole process of creating the geometry model and the positioning of the MRI measurements relative to the CFD results require tedious manual work. This fact raises the technical requirement of such extensive numerical studies involving multiple methods and becomes especially relevant for real-world engineering applications with complex flow domains.

A promising novel approach could be to obtain the flow domain from the velocity distribution by solving inverse problems. That is, an inverse Navier–Stokes problem is formulated as an optimization problem where the deviation between MRV and simulated velocity distribution is the target of optimization by adjusting the topology of the flow domain. This type of problem is addressed in the work of Kontogiannis et al. [30] where a Bayesian-optimization framework is used with a finite element method to solve the fluid dynamics. They additionally solved an inverse boundary value problem by reconstructing the velocity profiles at the domain edges. This was necessary as they addressed hemodynamic flow problems assessing, e.g., the wall shear stress at the arterial vessel wall, which is highly dependent on the inflow conditions [30]. The identical inverse Navier-Stokes problem was previously addressed by Klemens et al. [29] where they introduced a combined framework of adjoint formulation of the homogenized LBM proposed by Krause et al. [31–33] and gradient-based optimization. The theoretical background of the homogenized LBM originates from porous media flows and incorporates a scalar entity for a straightforward modeling of the fluid and solid phases inside the flow domain [34]. This property is utilized to adjust the topology of the fluid domain during the optimization process. By computing the sensitivities via adjoints, Klemens et al. successfully reduced the noise signals in two-dimensional velocity distributions measured by MRV [35]. While the deviation of the simulated and measured velocity distributions is minimized, the conservation equations restrict the optimized flow field, reducing the non-physical noise signals from the MRV data. Thus, this approach also compensates for the lower SNR at short measurement times [29,35].

Besides the difference in the applied methodologies in the works of Kontogiannis et al. [30] and Klemens et al. [29,35], the former conducted numerical experiments for only two-dimensional problems while the latter also computes three-dimensional simulations. The iterative nature of optimal flow control problems, i.e., computing several CFD simulations in each optimization cycle, demands high requirements on the numerical performance of the algorithms. In the context of addressing large-scale problems, as often required in three-dimensional flow control problems, the LBM is known for its efficient and effective discretization of conservation equations [36–40] due to its locality of computationally expensive operations as well as great scalability on GPUs [36,41–43]. In our previous work, the great synergy of LBM simulations in an iterative gradient-based optimization framework is demonstrated, where the forward mode of algorithmic differentiation computes the system sensitivities [27,44]. For distributed control variables such as in topology optimization problems, the LBM is often combined with adjoint sensitivity computation where the adjoint operators are derived either on the continuous or discrete level [29,36,42,45].

In the mentioned works addressing the inverse Navier-Stokes problem, their main focus was to improve the MRV image quality and not the reconstruction of the fluid domain as in the work of Klemens et. al [46]. The presented work is the continuation of [46], where the topology of three-dimensional geometrical shapes immersed in the flow field is identified. The inverse problem yields a permeability distribution containing the searched topology of the obstacle in the flow field, which can be translated into a 3D geometry model. They showed promising results reconstructing various geometrical shapes from simulated velocity distributions. Therefore, the long-term goal of the presented work is to explore an alternative approach to acquiring geometry models by utilizing the inverse Navier-Stokes problem. The advantages of this approach are (i) improvement of the image quality of MRV measurements,

(ii) avoiding the necessity of sophisticated methods of the data alignment as mentioned in [22] as the geometry model is recovered directly from the flow distribution, (iii) automated validation of the simulated flow field with the measured distribution, (iv) and on the long run, to omit CT-scan imaging by exploring an alternative approach in acquiring geometry models which reduces the technical hurdle for sophisticated numerical studies. While the previous work focuses on the proof of concept of the optimization framework by addressing academic-scale problems, this paper aims to investigate its capabilities to address real application cases, i.e., the topology identification of the OCF from MRV measurements. The aim of this paper is defined as follows:

- Investigation of the topology identification framework for various settings such as different Reynolds numbers, grid resolutions, and SNRs to identify optimal working conditions and restrictions/limitations of the framework
- Employment of the method on complex application case of the OCF using first simulation data and then 3D MRV data as the input of the framework
- Testing of the noise reduction capability and topology identification using CT-CFD as the ground truth

To the best of our knowledge, this is the first attempt to address the three objectives listed above. In order to achieve the aims in a structured manner, we formulate research questions as follows:

Q1: How does the framework react to different flow configurations regarding performance, accuracy, and robustness?
Q2: Is this method feasible to recover complex shapes like the OCF (using simulation data as input)?
Q3: What are the limitations/restrictions?
Q4: How does the method perform when experimental MRV data are fed to the framework?

The presented work is structured as follows. First, we formulate the inverse Navier-Stokes problem in Section 2. Then, Section 3 explains the optimization framework to solve the formulated problem. Section 4 introduces the utilized quality measures for quantifying the obtained results. Section 5 is about the interpretation of the recovered lattice porosity and permeability distributions in the context of the inverse flow problem. Next, in Section 6, numerical experiments to demonstrate the feasibility of the proposed method are conducted. First, the identification problem is solved using simulation data as input for the cuboid in Section 6.1 and then for the OCF in Section 6.2. Therein, various configurations regarding the grid resolution, Reynolds number, and SNR are investigated. Section 6.3 presents obtained results for the case where measured MRV data are used as the input for the inverse problem. Finally, Section 7 gives answers to the above formulated research questions followed by the conclusion in Section 8.

2. Problem formulation

The geometry acquisition problem in the current work is formulated as an inverse optimization problem where the deviation between measurements and their corresponding numerical model is the target entity of the minimization problem. Our method requires velocity data as its input to operate, i.e., the measure of success of the optimization problem is the difference in the velocity distributions. The optimization algorithm controls the permeability distribution in the numerical model, which represents the desired flow domain. Fig. 1 illustrates the presented approach to identify the foam structure in a tube probe from two perspectives. The black outer domain indicates the entire fluid domain Ω where the CFD simulation computes the flow field during a time interval I. It contains the simulation grid $\Omega_{\triangle x} \subseteq \Omega$ on which the velocity distribution $\mathbf{u} : \Omega_{\triangle x} \times I_{\triangle t} \to \mathbb{R}^d$ is computed, where $I_{\triangle t} \subseteq I$ is the discretized time domain. The blue color indicates the reference domain Ω^* where measured velocity distribution $\mathbf{u}^* : \Omega^* \to \mathbb{R}^d$ is available. Note that the spatial positions of the measurement data $\mathbf{x}^* \in \Omega^*$ do not necessarily correlate to the grid positions $\mathbf{x} \in \Omega_{\triangle x}$ in the simulation such that interpolation can be required to evaluate the deviation. The optimization algorithm adjusts the permeability of each numerical cell inside the design domain $\Omega^\alpha \subseteq \Omega^*$. A projection function connects the control variables $\boldsymbol{\alpha}$ and the permeability distribution, which will get further attention later in Section 3.1. The definitions of the length L and the diameter D of the tube probe, the length of the inflow L_{in} and outflow region L_{out} as well as the length of the foam structure L_{Ω^α} can be taken from Fig. 1.

To evaluate the success of the optimization problem, the *objective* of the inverse problem is defined as

$$\min_{\boldsymbol{\alpha}} J(f, \boldsymbol{\alpha}) = \frac{1}{2} \int_{\Omega^\alpha} (\mathbf{u}^* - \mathbf{u}(\alpha))^2 \mathrm{d}\mathbf{x}^*, \tag{1}$$

where f referrers to the *state* and $\boldsymbol{\alpha}$ to the *controls* of the optimization problem. Note, that (1) compares two velocity distributions which have reached steady state, explaining the missing integral over time in the equation. As the current optimization problem presents spatially distributed control variables, we differentiate the local control variable at a position $\mathbf{x} \in \Omega^\alpha$ by denoting as α and the serialized vector of all control variables by emphasizing in bold as $\boldsymbol{\alpha}$. The side constraint $\mathbf{G}$ establishes the connection between the local permeability to the velocity distribution via the continuity equation and the incompressible *Homogenized Navier-Stokes equation* (HNSE) [34], written as

$$\mathbf{G}(f, \boldsymbol{\alpha}) = \begin{cases} \boldsymbol{\nabla}_{\mathbf{x}} \cdot \mathbf{u}, \\ \partial_t \mathbf{u} + \mathbf{u} \cdot \boldsymbol{\nabla}_{\mathbf{x}} \mathbf{u} - \nu \boldsymbol{\Delta}_{\mathbf{x}} \mathbf{u} + \nu K(\alpha)^{-1} \mathbf{u} + \boldsymbol{\nabla}_{\mathbf{x}} p, \end{cases} \tag{2}$$

where $\nu > 0$ is the kinematic viscosity, $K : \Omega \to \mathbb{R}_{>0}$ is the local isotropic permeability, and $p : \Omega \times I \to \mathbb{R}_{>0}$ is the pressure. The goal of the optimization problem is to minimize (1) regarding the controls while fulfilling the constraints in (2), i.e., $\mathbf{G}(f, \boldsymbol{\alpha}) = \mathbf{0}$. This formulation of the optimization problem has been previously addressed in previous works for solving flow domain identification problems as in [29,31,35,46].

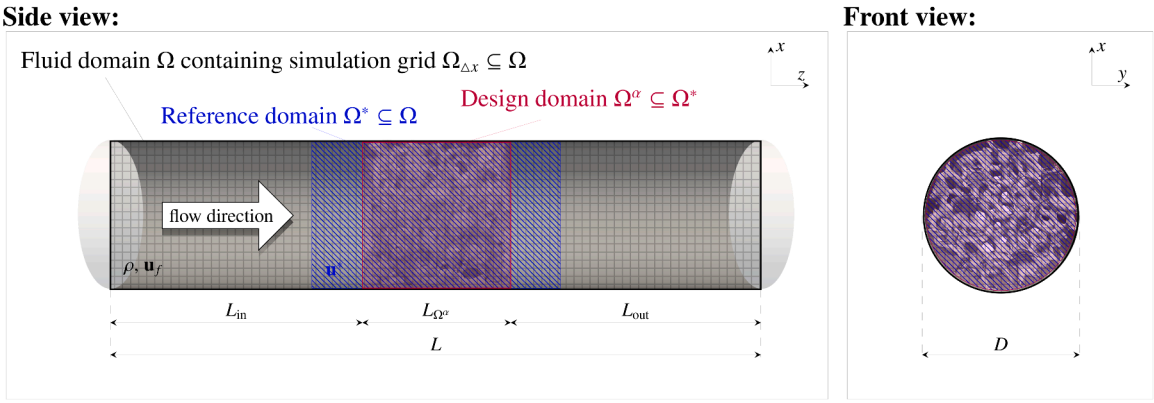

Fig. 1. Definitions of the various domains used in this work.

3. Solution strategy

In order to solve the optimization problem formulated in Section 2, a gradient-based optimization approach with a LBM scheme proposed by Krause et al. [31] is used. Therein, homogenization is applied to model the pressure loss due to the local permeability and its adjoint formulation derived on the continuous level such that this approach is a *first-optimize-then-discretize* approach according to [47]. For the optimization algorithm, limited memory Broyden-Fletcher-Goldfarb-Shanno (L-BFGS) [48] is used to compute the descend direction together with a step size control according to the Armijo-Wolfe-rule [47,48]. The lattice Boltzmann model to approximate (2) is presented in Section 3.1, as well as the adjoint formulation of that model to compute the objective gradients is shown in Section 3.2. The optimization algorithm and the workflow from velocity distribution to a geometry model are introduced in Sections 3.3 and 3.4, respectively.

3.1. Primal problem: homogenized Boltzmann model

The HNSE in (2) is approximated in the hydrodynamic limit via the *homogenized BGK-Boltzmann equation* (HBGKBE) [31], given as

$$\frac{\partial}{\partial t} f + \boldsymbol{\xi} \cdot \boldsymbol{\nabla}_{\mathbf{x}} f = \frac{1}{3\nu}(f - f_P^{\mathrm{eq}}) \quad \text{in } \Omega \times I \times \mathbb{R}^d, \tag{3}$$

where $f : \Omega \times I \times \mathbb{R}^d \to \mathbb{R}$ is the particle distribution function and $\boldsymbol{\xi} \in \mathbb{R}^d$ the particle velocity. The equilibrium distribution $f_P^{\mathrm{eq}} : \Omega \times I \times \mathbb{R}^d \to \mathbb{R}$ for the HBGKBE is given as

$$f_P^{\mathrm{eq}}(\mathbf{x}, t, \boldsymbol{\xi}) = \frac{\rho}{(2\pi RT)^{\frac{3}{2}}} e^{-\frac{1}{2RT}|\boldsymbol{\xi} - P\mathbf{u}|^2}, \tag{4}$$

where $\rho : \Omega \times I \to \mathbb{R}_{>0}$ is the density, R the ideal gas constant, and T the temperature. The porosity distribution $P : \Omega \to [0, 1]$ scales the local velocity at each position $\mathbf{x}$ with $P(\mathbf{x}) = 0$ for completely solid, $P(\mathbf{x}) = 1$ for fluid only, and $0 < P < 1$ for porous positions [29].

By discretization of (3) with the *lattice Boltzmann method* (LBM), we obtain the *homogenized lattice BGK-Boltzmann equation* (HLBGKBE), written as

$$f_i(\mathbf{x} + \boldsymbol{\xi}_i \triangle t, t + \triangle t) - f_i(\mathbf{x}, t) = \frac{\triangle t}{\tau}(f_i(\mathbf{x}, t) - f_{P,i}^{\mathrm{eq}}(\mathbf{x}, t)) \quad \text{in } \Omega_{\triangle x} \times I_{\triangle t}, \tag{5}$$

for $i \in 0, 1, \ldots, Q-1$ with Q discrete particle velocity directions corresponding to the velocity model $D3Q19$. Here $f_i : \Omega_{\triangle x} \times I_{\triangle t} \to \mathbb{R}$ is the discrete particle distribution function, which is defined on a homogeneous grid with a step size $\triangle x \in \mathbb{R}$ at discrete time steps $\triangle t \in I_{\triangle t}$. The discrete equilibrium distribution $f_{P,i}^{\mathrm{eq}} : \Omega_{\triangle x} \times I_{\triangle t} \to \mathbb{R}$ is given for the $D3Q19$ velocity model as

$$f_{P,i}^{\mathrm{eq}}(\mathbf{x}, t) = w_i \rho \left(1 + \frac{\boldsymbol{\xi}_i \cdot P\mathbf{u}}{{c_s}^2} - \frac{(P\mathbf{u})^2}{2{c_s}^2} + \frac{(\boldsymbol{\xi}_i \cdot P\mathbf{u})^2}{2{c_s}^4}\right), \tag{6}$$

where w_i are weights corresponding to the $D3Q19$ model as given in [36], and $c_s = 1/\sqrt{3}\frac{\triangle t}{\triangle x}$ the lattice speed of sound. In this work, we apply diffusive scaling for the discretization parameters, i.e. $\triangle t \sim \triangle x^2$. The following relation connects the lattice porosity with the local permeability given as [34]

$$P(\mathbf{x}) = 1 - \frac{G_h}{K}, \quad \text{with } G_h = \triangle x^2 \nu \tau. \tag{7}$$

Since the porosity in (7) is bounded to $[0, 1]$, the permeability limited to $[G_h, \infty)$. Klemens et al. [35] introduced a projection to establish the connection between the local control variable and the local permeability while fulfilling $\mathcal{B} : \mathbb{R} \to [0, \infty)$ with $K = \mathcal{B}(\alpha) +$

G_h. In this work the exponential function is chosen for $\mathcal{B}$ as in [35], leading to the following connection between porosity and control:

$$P(\alpha) = \frac{e^{\alpha}}{e^{\alpha} + G_h}. \tag{8}$$

As (8) is identical to the Sigmoid function up to a translation in the projection, the Sigmoid function is used directly for simplicity instead. Finally, the macroscopic density and velocity can be recovered over the statistic moments, given as

$$\rho(\mathbf{x}, t) = \sum_{i=0}^{Q-1} f_i, \quad \text{and} \quad \mathbf{u}(\mathbf{x}, t) = \rho^{-1} \sum_{i=0}^{Q-1} \boldsymbol{\xi}_i f_i, \tag{9}$$

where $Q \in \mathbb{N}$ is the number of discrete velocities of the velocity discretization model.

3.2. Adjoint problem: adjoint homogenized Boltzmann model

To apply gradient-based optimization, the derivative of the objective from (1) regarding the controls $\mathrm{d}J/\mathrm{d}\boldsymbol{\alpha}$ becomes necessary. Krause et. al [31] derived an adjoint formulation of the HBGKBE in (3) on the continuous level, namely the *adjoint homogenized BGK-Boltzmann equation* (AHBGKBE), given as

$$-\frac{\partial}{\partial t}\varphi - \boldsymbol{\xi} \cdot \boldsymbol{\nabla}_{\mathbf{x}}\varphi = \frac{1}{3\nu}(\varphi - \varphi_P^{\mathrm{eq}}) + \frac{\partial}{\partial f} J \quad \text{in } \Omega \times I \times \mathbb{R}^d, \tag{10}$$

where $\varphi : \Omega \times I \times \mathbb{R}^d \to \mathbb{R}$ are the adjoints and with the adjoint equilibrium distribution, defined as

$$\varphi_P^{\mathrm{eq}}(\mathbf{x}, t) = \frac{1}{\rho} \int_{\mathbb{R}^d} \varphi(\hat{\boldsymbol{\xi}}) f_P^{\mathrm{eq}}(\hat{\boldsymbol{\xi}})(1 + 3P(\hat{\boldsymbol{\xi}} - P\mathbf{u}) \cdot (\boldsymbol{\xi} - \mathbf{u}))\, \mathrm{d}\hat{\boldsymbol{\xi}}. \tag{11}$$

The source term after the adjoint collision term in (10) is given as [34]

$$\frac{\partial}{\partial f} J(f, \boldsymbol{\alpha}) = \frac{(\mathbf{u}(\alpha) - \mathbf{u}^*) \cdot (\boldsymbol{\xi} - \mathbf{u}(\alpha))}{\rho}, \tag{12}$$

where the converged macroscopic entities of the primal problem in (3) are inserted. Note that for the derivation of the AHBGKBE, the formulation of the objective function additionally contains the integration over time to account for in-stationary problems. However, previous works demonstrated that this scheme can be applied straight forward to stationary problems, cf. [29,31,35,46]. Due to the similar structure of the AHBGKBE in (10) to its primal formulation in (5), it can be discretized by an LBM, leading to the *adjoint homogenized lattice BGK-Boltzmann equation* (AHLBGKBE), written as

$$\varphi_i(\mathbf{x} - \boldsymbol{\xi}_i \triangle t, t - \triangle t) - \varphi_i(\mathbf{x}, t) = \frac{\triangle t}{\tau}(\varphi_i - \varphi_{P,i}^{\mathrm{eq}}) + \frac{(\mathbf{u} - \mathbf{u}^*) \cdot (\boldsymbol{\xi}_i - \mathbf{u})}{\rho} \quad \text{in } \Omega_{\triangle x} \times I_{\triangle t}, \tag{13}$$

for $i = 0, 1, \ldots, Q-1$, where the discrete adjoint equilibrium distribution is given as

$$\varphi_{P,i}^{\mathrm{eq}}(\mathbf{x}, t) = \frac{1}{\rho} \sum_{j=0}^{Q-1} \varphi_j (1 + 3P(\boldsymbol{\xi}_j - P\mathbf{u}) \cdot (\boldsymbol{\xi}_i - \mathbf{u})) f_{P,j}^{\mathrm{eq}}. \tag{14}$$

The macroscopic density and velocity in (14) are computed using the stationary solution of the primal problem of (5). Finally, by using the stationary results of (5) and (13), the total derivative of the objective regarding the control variable can be computed via

$$\frac{\mathrm{d}J}{\mathrm{d}\alpha} = -\frac{\mathbf{u}}{{c_s}^2 \tau} \frac{\partial P}{\partial \alpha} \sum_{i=0}^{Q-1} \varphi_i f_{P,i}^{\mathrm{eq}} (\boldsymbol{\xi}_i - P\mathbf{u}) \quad \text{in } \Omega^{\alpha}, \tag{15}$$

Due to the lattice-Boltzmann discretization of the primal and adjoint problem, both equations can utilize the high affinity towards parallelization, exploiting high-performance computing resources for simulating fluid flow and computing distributed sensitivities [29, 31].

The boundary conditions in the adjoint simulation depend on their primal counterpart. That is, the primal boundary treatment needs to be incorporated into the derivation of the adjoint equations. Interested readers are referred to [45] or [49]. In the present manuscript, we assume negligible sensitivity coming from the boundary as the Reynolds number is relatively low and the boundary is not controlled nor the objective functional is evaluated at the boundary, similar to [49].

3.3. Gradient-based line search algorithm

The complete algorithm to solve the inverse problem formulated in Section 2 is shown in Algorithm 1. First, the permeability inside the entire design domain Ω^{α} is prescribed according to the initial guess α^0 as a starting point of the topology identification problem. Then, the terminating condition needs to be specified. Typically, the algorithm terminates when the total derivative of the objective regarding the controls, i.e., $\mathrm{d}J/\mathrm{d}\boldsymbol{\alpha}$ is below a user-specified threshold ϵ. As alternative termination conditions, one can set the maximal number of allowed iterations $m_{\max}$ and $k_{\max}$ for the optimization and step control, respectively. The primal problem introduced in (5) is solved until it reaches a steady state regarding the average flow velocity. The particle distribution functions

from the primal simulation provide the macroscopic density and velocity, which are required to compute (14) and the force term in (13). Then, the algorithm simulates the adjoint problem until convergence [46] to obtain the necessary objective sensitivities for (15). Note that the time integration of the objective in (1) can be omitted for stationary problems as shown in [29,35,46]. We use L-BFGS [48] to compute the descent direction $s^{m,k}$ where the function evaluations of the last 20 optimization steps are stored to enable quick convergence against the optimal solution. For an efficient gradient descent method, a step control is applied according to Armijo-Wolfe-rules [47,48]. That is, the rule checks each computed step width to satisfy a sufficient decrease in the optimization objective and its gradient, balancing the stability and performance of the optimization algorithm. After obtaining a valid step width, the controls are updated, and the algorithm proceeds with the following optimization step $m+1$ until exiting through the terminating condition.

Algorithm 1 Gradient-based (Adjoint-based) optimization algorithm with step control.

procedure MINIMIZE($J(f, \boldsymbol{\alpha})$)
  Choose initial guess α^0, maximal number iterations $m_{\max}, k_{\max}$, and convergence tolerance ε
  repeat ▷ For $m = 0, 1, 2, \dots, m_{\max}$
    Solve primal problem until convergence ▷ (5)
    Solve adjoint problem until convergence ▷ (13)
    Compute $\mathrm{d}J/\mathrm{d}\alpha$ using results from step 4 and 5 ▷ (15)
    Compute descent direction via L-BFGS using result from step 6
    repeat ▷ For $k = 0, 1, 2, \dots, k_{\max}$
      Choose new step size $s^{m,k}$
      Check if valid step for $\delta\boldsymbol{\alpha}^{m,k} = s^{m,k}\mathbf{d}^m$ ▷ (5) / (13)
    until Valid step size found **or** $k = k_{\max}$
    Update controls $\boldsymbol{\alpha}^{m+1} = \boldsymbol{\alpha}^m + \delta\boldsymbol{\alpha}^m$
  until $J(f^m, \boldsymbol{\alpha}^m) < \varepsilon$ **or** $(\mathrm{d}J/\mathrm{d}\boldsymbol{\alpha})(f^m, \boldsymbol{\alpha}^m) < \varepsilon$ **or** $m = m_{\max}$ ▷ Terminating condition
end procedure

3.4. Geometry reconstruction workflow

The velocity distributions simulated or measured by MRV are stored in the VTI data-format[1] and provide the velocity vectors given in m/s as cell-averaged values in a structured grid with uniform spacing. The velocity data are read node-wise in OpenLB [36] such that for each grid position $\mathbf{x} \in \Omega^*$, the corresponding cell is looked up with its velocity $\mathbf{u}^*$ to compute (1) and (15). The simulation domain matches the measurement, i.e., the flow domain has a cylinder-shaped geometry with the reference and design domain residing inside as illustrated in Fig. 2. From the experimental setup, the bounding box for the design domain is set. To archive similarity of the flow field, the Reynolds number is set as in the experimental setup. The inflow and outflow distance is set large enough to neglect undesired boundary influences, whereas at the inflow a parabolic velocity profile and at the outflow a constant pressure is prescribed in the simulation.

After solving the inverse problem, a geometry model is obtained from the computed porosity distribution by extracting a level surface for a porosity threshold. Additionally, the optimization objective directly delivers the distance between the two velocity distributions. The level surface can be then exported as a surface mesh for following numerical investigations.

4. Quality measures

This section introduces the quality measures to assess the accuracy of the reconstructed flow domain and of the resulting velocity distribution.

[1] VTK - The Visualization Toolkit 9.3., Kitware, USA, https://vtk.org/.

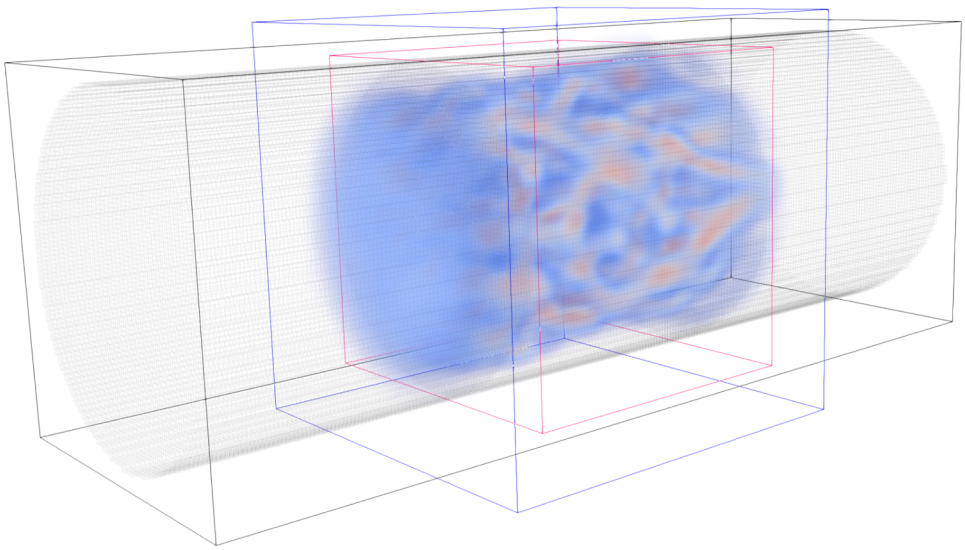

Fig. 2. Positioning of the MRV measurement data in the simulation domain. The black, blue, and red boxes denote the outlines of the discretized flow domain $\Omega_{\triangle x}$, domain for the reference velocity distribution Ω^*, and design domain Ω^α, respectively. (For interpretation of the references to colour in this figure legend, the reader is referred to the web version of this article.)

Table 1
Cell-wise binary classification cases for the identified outcome.

Outcome \ Reference	Solid ($P^* = 0$)	Fluid ($P^* = 1$)
Solid ($P \leq P_T$)	**True Solid (TS)** Correctly identified solid	**False Solid (FS)** Overestimated as solid
Fluid ($P > P_T$)	**False Fluid (FF)** Underestimated as fluid	**True Fluid (TF)** Correctly identified fluid

4.1. Velocity distribution

To assess the deviation between the reference velocity and the recovered velocity distribution, the relative error as a weighted expression of the discrete objective functional from (1), i.e., the L^2-norm over the design domain is used, given as

$$||\Delta \mathbf{u}||^{\text{rel}}_{L^2(\Omega^\alpha)} = \sqrt{\frac{\sum_{\mathbf{x}\in\Omega^\alpha}(\mathbf{u}^* - \mathbf{u})^2}{\sum_{\mathbf{x}\in\Omega^\alpha}\mathbf{u}^{*2}}}. \tag{16}$$

4.2. Geometry model

To assess the quality of the reconstructed flow domain, we make use of (7) to translate the permeability interchangeably into a lattice porosity. The bounded interval of $P \in [0, 1]$ allows a simple definition of solid or impermeable cell with $P = 0$ and fluid or permeable cell with $P = 1$. In the following numerical experiments, the reconstructed geometry model is compared against the geometry obtained from CT-scan images. The CT-scan model is translated into a binary distribution of lattice porosity values depending whenever a cell is inside or outside of the solid object. This binary reference porosity field is used to validate the reconstructed porosity distribution. We avoid to use the L^2-norm to compute the error between the two porosity or permeability distributions as the lattice porosity is grid-dependent and the permeability is affected by the Reynolds number. These aspects are discussed in the following section more in detail. A more general way of assessing the quality of the identified topology is to use a binary classification method as in [50]. As the optimal result contains only discrete values zero or one regarding the lattice porosity, a threshold P_T decides the identification outcome accordingly to the cases shown in Table 1.
Upon those four possible cases, the Jaccard index, also referred to as the similarity index, is computed as the quality measure for the reconstructed topology [51]. It gives the similarity of two objects, i.e., a measure of intersection over union. That is, for two sets A and B it is defined as $\text{Jaccard}(A, B) = |A \cap B|/|A \cup B|$ with $\text{Jaccard} \in [0, 1]$, giving in our case:

$$\text{Jaccard} = \frac{\text{TS}}{\text{TS} + \text{FS} + \text{FF}}. \tag{17}$$

The identified lattice porosity distribution by the optimization framework is discrete in the optimal case, meaning consisting of values either being zero or one. Generally, this is not the case such that a distribution of lattice porosity values in $[0, 1]$ is found. If the

inverse problem formulation is well-posed, that is, a clear separation of solid cells from fluid cells by the optimization framework is possible, the resulting lattice porosity distribution approaches a bimodal distribution like the Bernoulli-distribution. To assess if the recovered distribution is close to the ideal distribution, the bimodality coefficient $B \in [0,1]$ is computed as [52]

$$B = \frac{m_3^2 + 1}{m_4 + \frac{3(n-1)^2}{(n-2)(n-3)}}, \tag{18}$$

where m_3 is the skewness, m_4 is the kurtosis, and n the probe size, which in our case is equal to the number of design variables N_{Ω^α}.

Finally, to allow the comparison of two distributions which were not binary, e.g., for the signal amplitude image measured by MRI and the reconstructed porosity distribution, the Pearson correlation coefficient (PCC) is used [53], given as

$$\mathrm{PPC} = \frac{\mathrm{cov}(\mathrm{W}_1, \mathrm{W}_2)}{\sigma_{\mathrm{W}_1} \sigma_{\mathrm{W}_2}}, \tag{19}$$

where $\mathrm{cov}(\mathrm{W}_1, \mathrm{W}_2)$ is the covariance of the two geometry distributions and σ_{W_1} and σ_{W_2} the standard deviations of the distributions W_1 and W_2, respectively.

All measures regarding the geometry quality are computed by using the distributions inside the design domain Ω^α.

4.3. System sensitivity

The L^2-norm regarding the total derivative of the optimization objective over the local control gives a measure for the sensitivity of the system

$$\left|\left| \frac{\mathrm{d}J}{\mathrm{d}\alpha} \right|\right|_{L^2(\Omega^\alpha)} = \sqrt{\sum_{\mathbf{x} \in \Omega^\alpha} \left(\frac{\mathrm{d}J}{\mathrm{d}\alpha} \right)^2 \triangle x^d}, \tag{20}$$

where this value tends to zero when approaching to a local minima. This value is used to check whenever to terminate gradient-based optimization problems. In the presented work, the threshold regarding (20) is set to 10^{-17}. The algorithm is terminated either (20) is below the threshold or the number of optimization steps succeeds $m = 100$, if not stated differently.

5. Interpretation of the reconstructed lattice porosity distribution

One central question regarding the computed lattice porosity distribution remains, that is, how to convert the continuous range of values between zero and one into a binary distribution, or more specifically, what value for the porosity threshold P_T leads to the most accurate geometry model. To answer this, we need to know when a grid-cell can be considered as *quasi-impermeable for the flow field* in terms of the inverse problem. This can be also rephrased into *for what lattice porosity/permeability a cell behaves basically solid for the flow* as the objective only considers the velocity deviation. This section is dedicated to give an interpretation of the inversely identified lattice porosity/permeability by the inverse flow problem and contains a pre-study investigating the suitability of a novel measure which gives for what permeability a cell acts basically as impermeable.

5.1. Lattice porosity and permeability

The approximated HNSE in (2) can model a rigid, impermeable obstacle in the flow via introducing a pressure loss by the Darcy force $\nu \mathbf{u}/K$ in the limit of $K \to 0$. The Eq. (7) shows that by setting $P = 0$ the permeability is equal to G_h which is proportional to the spatial grid resolution in the power of two. Furthermore, the Darcy force depends on the flow velocity and viscosity. This shows three important aspects which becomes relevant when solving inverse topology identification problems using HLBM:

- The grid-dependency of the lattice porosity,
- the existence of minimal permeability for a certain spatial resolution, namely $K_{\min} = G_h$, and
- the Reynolds number dependency of Darcy force in the HNSE.

The first aspect has been properly addressed in the prior work of Klemens et al. [35] where the grid-independence of the permeability is shown and a projection is constructed which ensures the link to the control variable. However, for a suitable choice of P_T this remains a problem as the lattice porosity is grid-dependent. The natural following would be to use the permeability, which is known to be independent of discretization parameters, instead of the lattice porosity to find P_T. Nevertheless, the second and third aspect listed above will demonstrate that the permeability has its own implications. The second aspect has been addressed in the work of [54] where it is shown, that the HLBM produces higher numerical errors regarding the pressure drop when the lattice porosity approaches zero, or $K \to K_{\min}$. Eq. (6) shows that for $P = 0$, the first moment is zero meaning that the velocity of that lattice cell is equal to zero. However, inserting $P = 0$ into (7) yield $K_{\min} = G_h(\triangle x^2)$ showing that only in the limit of $\triangle x \to 0$ the permeability approaches zero for $P = 0$. When HLBM is used to model porous media flows, the permeability can be set according to the material properties of the porous media and as $K_{\min} \to 0$ with $\mathcal{O}(\triangle x^2)$ the model becomes consistent. Now, as we want to determine when a cell can be considered impermeable for the flow field in the inverse problem, one approach could be to estimate the permeability K^* where a cell is nearly impermeable, e.g., the volume flux through the cell is sufficiently close to zero. However, if the grid resolution is not sufficient in terms of $K_{\min} > K^*$, the volume flux can be still set to zero when $P \approx 0$. This discrepancy explains the higher numerical

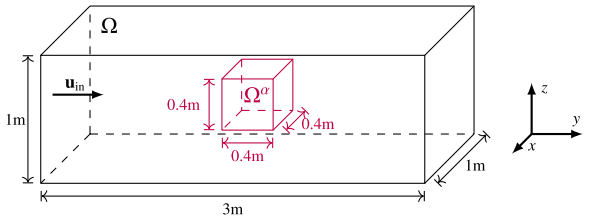

Fig. 3. Set up cuboid simulation case.

error shown in [54] for $K \to K_{\min}$. This fact complicates the correct interpretation of the reconstructed permeability and makes it challenging to choose a suitable K^* for choosing a suitable porosity threshold P_T. Simply increasing the grid resolution to reach lower $K_{\min}$ is unfortunately not an option as the grid resolution not only impacts on the computation time but also on the outcome of the inverse problem as we will see later. The third aspect becomes particularly interesting in the current study as one of the aims is to investigate the behavior of the presented method for different Reynolds numbers which is a contrast to the prior work [46] where only a single flow rate is concerned. The appearance of the flow velocity and viscosity in the Darcy term in (2) indicates the dependency of the Reynolds number on the Darcy force. As the Darcy force impacts on the flow distribution, this could imply that depending on the Reynolds number the identical permeability value has different influence on the flow, i.e., different sensitivity to the objective. To address this concern, dimensionless variables are introduced and inserted in the HNSE. By replacing the reference time and pressure via the remaining variables, the momentum balance law of the HNSE can be written in the dimensionless form as

$$\partial_t \mathbf{u} + \mathbf{u} \cdot \boldsymbol{\nabla}_{\mathbf{x}} \mathbf{u} - \frac{1}{\mathrm{Re}} \nu \boldsymbol{\Delta}_{\mathbf{x}} \mathbf{u} + \frac{1}{\mathrm{ReDa}} \nu K(\alpha)^{-1} \mathbf{u} + \boldsymbol{\nabla}_{\mathbf{x}} p, \tag{21}$$

where $\mathrm{Re} = \mathbf{u} L / \nu$ is the Reynolds number and $\mathrm{Da} = K / L^2$ is the Darcy number. This confirms the dependency of the Darcy force on the Reynolds number and lead to the fact that we might need to adjust the P_T for each flow rate.

To summarize, to find the suitable P_T based on the lattice porosity or the permeability have implications due to the grid-dependency or flow-rate dependency, respectively. These dependencies are also the reason why we avoid to assess the quality of the reconstructed flow domain based on the L^2-error of the porosity/permeability distributions.

5.2. Relative velocity norm

We propose to directly assess the impact of the porosity/permeability on the flow field based on the resulting velocity distribution. For this, a numerical experiment is conducted where the impact of a cell immersed in the flow field with a certain permeability is evaluated for a range of Reynolds and Darcy numbers. This numerical test case is set up similarly as in [46] and shown in Fig. 3 where a cuboid with a side length of $L_{\Omega^\alpha} = 0.4\mathrm{m}$ and a uniform permeability is positioned in the center of a channel as depicted. At the inflow, a homogeneous velocity distribution $\mathbf{u}_{\mathrm{in}}$, at the outflow a constant pressure is prescribed via setting the missing values to the equilibrium distribution with the desired macroscopic values [55]. The remaining walls apply bounce-back for the boundary treatment, the relaxation time is set to $\tau = 0.7$ and resolution of the object to $N_{\Omega^\alpha} = 24$ in all simulations. The Reynolds and Darcy number is varied for the simulation where $Re = \mathbf{u}_{\mathrm{in}} L_{\Omega^\alpha} / \nu$ and $Da = K / {L_{\Omega^\alpha}}^2$. To measure the impact on the velocity field, the relative ratio of the L^2-norm inside the object is evaluated which is defined as [46]

$$\mathrm{RVN} = \frac{||\mathbf{u}||_{L^2(\Omega^\alpha)}}{||\mathbf{u}_\infty||_{L^2(\Omega^\alpha)}}, \tag{22}$$

where $\mathbf{u}_\infty$ is the case where the lattice porosity of the object is set to $d = 1$ which leads to a vanishing Darcy force. This norm will be referred to in the following as the relative velocity norm (RVN). In the incompressible and unidirectional case (22) is equal to the relative mass flow through the cell compared to the free stream case. The RVN is computed for Darcy numbers ranging from $[10^{-5}, 10^{1}]$ and Reynolds numbers from $[10^{-2}, 10^{2}]$ where on the logarithmic scale 20 evenly distributed values are simulated for each variable resulting in total 400 simulations. This is visualized in Fig. 4 where contour lines are added on top of the surface plot. It can be observed, that above $Re > 10^0$ the same permeability has less impact on the flow field for increasing the flow rate, i.e., lower RVN for higher Reynolds number. This means, if a cell can be considered being impermeable for the fluid for example at $\mathrm{RVN} = 10^{-2}$, for higher Reynolds numbers a lower permeability becomes necessary leading the lattice porosity to approach zero. This matches the physical expectations as a higher Darcy force is required for higher Reynolds numbers. With the RVN, we obtained a measure of how impermeable a cell is for the flow field at the recovered lattice porosity/permeability in the inverse problem including the effects of the current flow rate.

6. Results

This section presents the numerical results of the presented framework to solve flow domain identification problems. First, Section 6.1 introduces the identification of a cuboid object as shown in Fig. 3. Therein, the influence of the grid resolution and the Reynolds number is investigated. Then, in Sections 6.2 and 6.3 the framework is applied on the more complex geometry, the

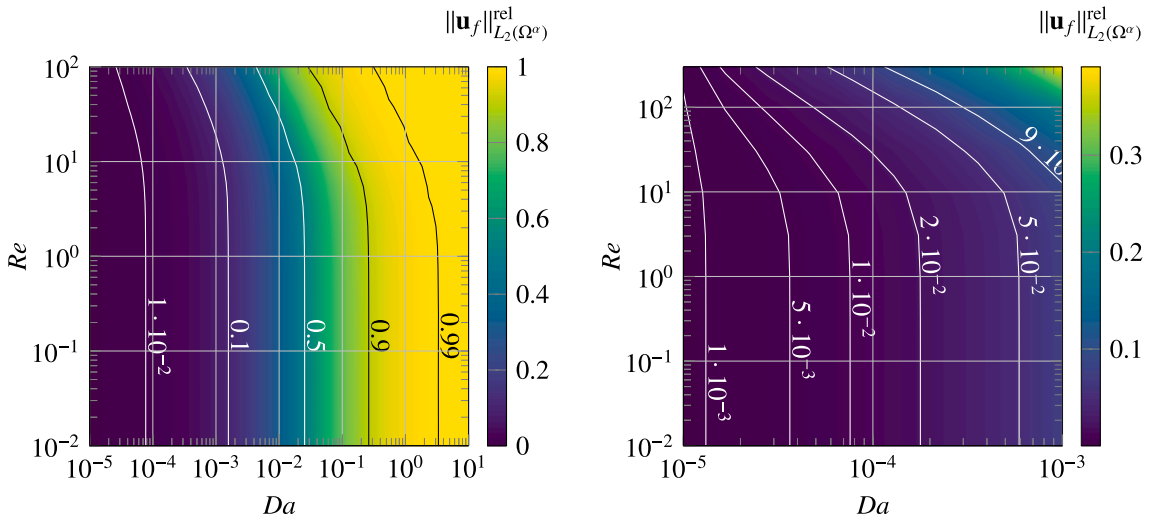

(a) 20×20 simulation for $Re \in [10^{-2}, 10^{2}]$ and $Da \in [10^{-5}, 10^{1}]$.

(b) 10×10 simulation for $Re \in [10^{-2}, 10^{2}]$ and $Da \in [10^{-5}, 10^{-3}]$.

Fig. 4. Reynolds number and Darcy number dependency on the RVN in (22). Contour lines for exemplary values are highlighted. The dependency of the Reynolds number on the flow field for a constant Darcy number is demonstrated.

OCF. The foam geometry is reconstructed in the former section from simulated velocity distribution and in the latter from MRV measurements. Different influences are addressed in Section 6.2 such as Reynolds number, grid resolution, and artificial noise signals. Section 6.3 starts with the experimental set up of the MRV measurement followed by the numerical results. All numerical results are produced using OpenLB on a local setup consisting of one socket Intel Xeon Gold 6326 CPU with 16 cores and 64 GiB of memory. This is complemented by two NVIDIA RTX A5000 GPUs, each equipped with 24 GiB of memory. The GPUs were interconnected via NVLink, and OpenMPI is used for communication between the GPUs. O3 compiler optimization and common sub-expression elimination (CSE) is employed for the primal and dual collision models, ensuring efficient code execution and reduced computational overhead.

6.1. Topology identification of a cuboid from simulation data

The reconstruction of the cuboid is simulated first for $Re = 1$ where the viscosity is set to $\nu = 0.4\,\text{m}^2/s$ and the velocity to 1 m/s. The characteristic length is resolved with $N = 8$, 16, 24, and 32. The reference domain is a cuboid with the side length of $L_{\Omega^*} = 1\,\text{m}$ where in its center Ω^α resides where the reference velocity is available to compute the objective and gradients. All the other simulation parameters are set identical as in the experiment conducted in Section 5. A reference simulation with porosity values zero for the cuboid obstacle and one for the remaining flow field is conducted and its resulting velocity field used as the input for the optimization algorithm. The initial permeability distribution inside of the design domain has been chosen to $K = 0.01\,\text{m}^2$.

Fig. 5a shows the relative L^2-error regarding the flow velocity over the optimization steps for the computed resolutions. It can be clearly seen that the curve is almost identical for all the resolutions, indicating the independence of the reconstructed solution in terms of the flow distribution by the optimization problem. This demonstrates the correct working of the proposed projection between the lattice porosity and control variable over the permeability proposed in [35]. The relative error of the velocity starts at the initial step with 40% and reduces to 1% after 10 optimization steps. This continues up to a remaining error of 0.1% for $N = 32$ after 100 optimization steps which corresponds to a reduction of a factor of 400 compared to the initial error. The Jaccard index is plotted in Fig. 5b over the optimization steps showing the great recovery of the cuboid geometry where for resolutions above $N = 16$ the Jaccard index yields ≥ 0.99. Similarly, to the relative error in the velocity the optimization framework recovers the topology of the cuboid already up to a Jaccard index of ≥ 0.8 in the first 10 optimization steps. After 60 optimization steps only incremental improvement of the index is observable. Table 2 shows the quality measures of the recovered topology for the various resolutions at the final successful optimization step. The accuracy of the prediction of solid and fluid cell is demonstrated using the binary classification where for all resolutions the percentage of correctly identified solid cells over all solid cells exceeds 0.98% for the chosen porosity threshold.
In Fig. 5b the curves do not align for the various resolution. The reason for this is illustrated in Fig. 6a, where a contour plot for the reconstructed lattice porosity for $N = 32$ is shown in the y-z-plane together with the velocity field. Therein, the outer boarders of the cuboid is identified clearly but the appearance of intermediate lattice porosity values in the inside of the object shows ambiguity issues of the optimization problem as those cells do not have any influence on the fluid flow field. Fig. 6b presents the Jaccard index over the lattice porosity threshold which is used for the binary classification in Table 1. A tendency of increasing ambiguity issues in the inside of the cuboid for increasing resolution can be observed as the interval leading to the highest Jaccard index gets narrower. The Bimodality index in Table 2 supports the findings as the lowest resolution has the closest value to one,

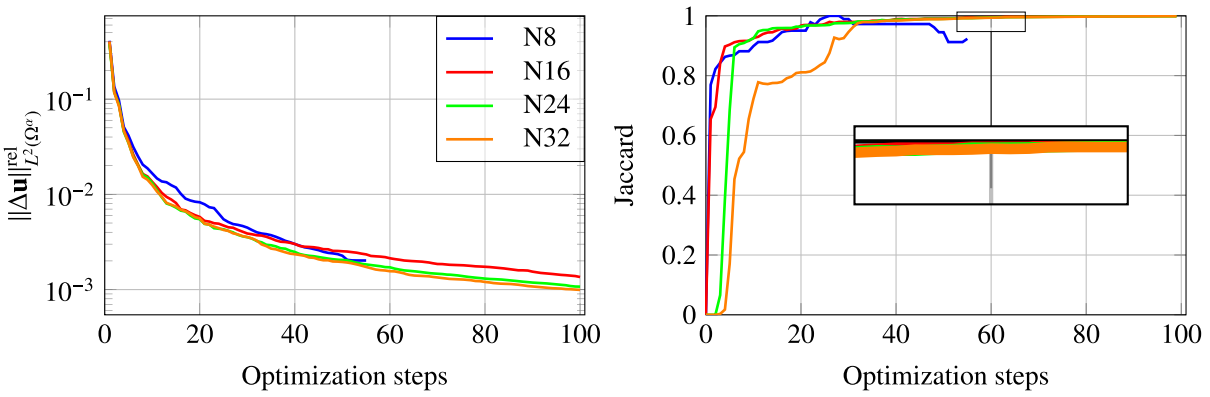

(a) Relative velocity error over the optimization steps. Logarithmic scale is employed for the y-axis.

(b) Jaccard index computed for a porosity threshold of $P_T = 0.9$ over the optimization steps.

Fig. 5. Quality measures for the reconstructed velocity and identified topology in the cuboid case with $Re = 1$. Grid independence is demonstrated regarding the relative velocity error.

Table 2
Quality measures of the identified cuboid topology for various resolutions with $Re = 1$. For the definition of the binary classification refer to Table 1.

N	Jaccard	P_T	TS	TF	FS	FF	B
8	0.96	0.99	713	6840	12	16	0.995
16	1.00	0.88	4914	57,447	0	0	0.979
24	0.99	0.86	15,625	196,694	22	0	0.939
32	0.99	0.84	35,937	469,534	50	0	0.925

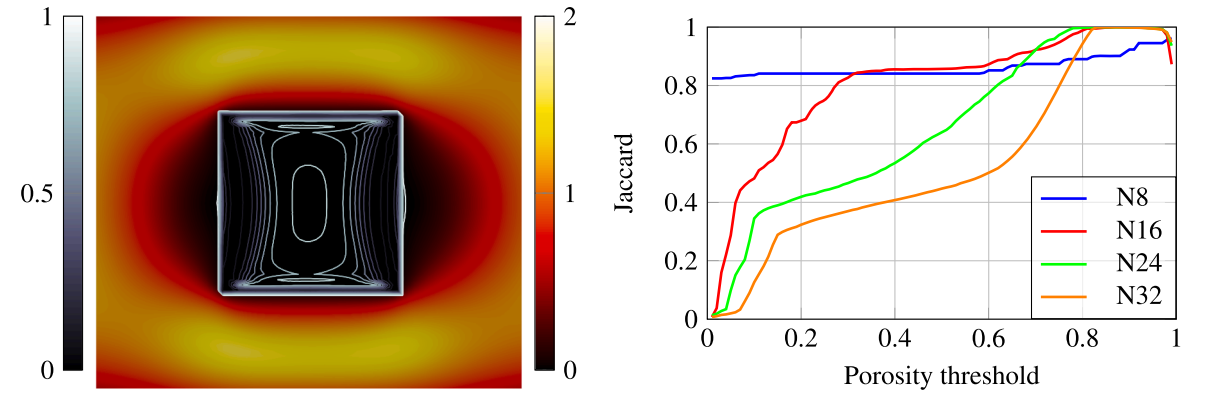

(a) Contour plot of the reconstructed lattice porosity after 100 optimization steps. The left color bar represents the lattice porosity and the right color bar the flow velocity in m/s.

(b) Jaccard index over the lattice porosity threshold.

Fig. 6. Ambiguity issues in the inside of the cuboid geometry is depicted on the right. This increases the difficulty in finding a suitable porosity threshold to compute the Jaccard index as shown in the left.

indicating the best separation of solid and fluid cells over the whole lattice porosity distribution. Thus, the Bimodality index can be also interpreted as an indicator of the occurrence of ambiguity issues in the form of intermediate lattice porosity values in the recovered solution. At the front side of the cuboid facing upstream, a homogeneous permeability of $K_{\text{front}} = 1.28 \times 10^{-5}\,\text{m}^2$ is computed for the resolutions $N = 16, 24, 32$. Referring to Fig. 4 a homogeneous cuboid with the same permeability leads to a RVN of $\approx 1\%$. For $N = 8$, the reconstructed permeability is higher leading to a RVN of 5% which is due to the limit of $K_{\text{min}} \approx G_h$ as mentioned in Section 5. The constant RVN, computed from the permeability obtained at the surface facing upstream, indicates that for a corresponding permeability leading to a RVN of $\approx 1\%$ a cell behaves quasi-impermeable for the flow and thus found by the inverse problem.

Table 3
Quality measures of the identified cuboid topology for various Reynolds number with $N = 24$. For the definition of the binary classification refer to Table 1.

Re	$\|\|\Delta\mathbf{u}\|\|^{\text{rel}}_{L^2(\Omega^e)}$	Jaccard	P_T	TS	TF	FS	FF	B
1	0.15%	0.99	0.86	15,625	196,694	22	0	0.939
10	0.18%	0.96	0.9	15,625	196,112	604	0	0.999
20	0.20%	0.93	0.99	14,810	196,447	269	815	0.996

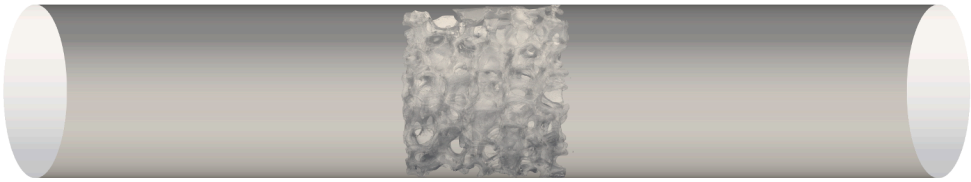

(a) STL geometry created from the CT scan images. The OCF is the placed into an pipe geometry.

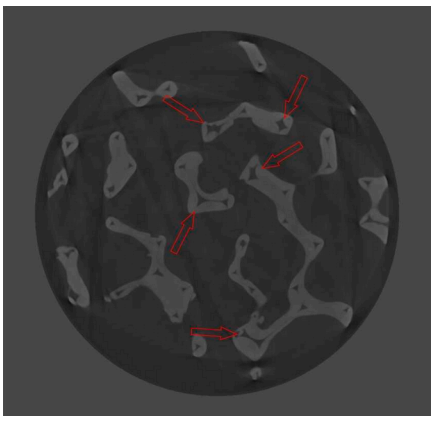

(b) Exemplary CT scan image showing the cavities inside the foam strut highlighted by red arrows.

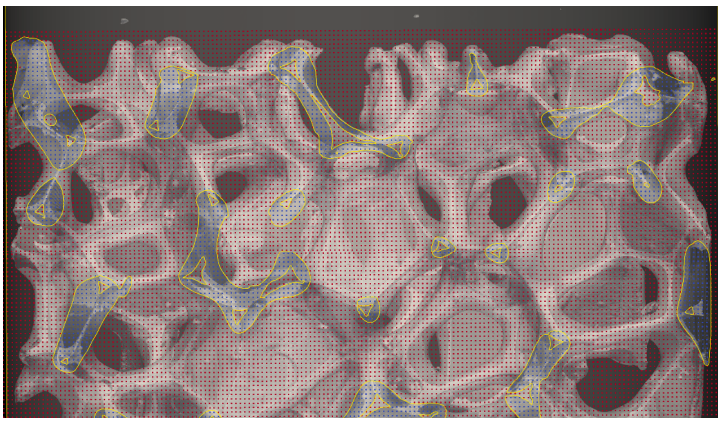

(c) Obtained reference lattice porosity distribution with red cells as fluid cells and blue cells as solid cells. The yellow lines show the cut STL geometry.

Fig. 7. Acquisition of the reference lattice porosity distribution used for computing the reference velocity distribution for the topology identification of OCF. From the CT scan image stacks the STL model is created wherein inner cavities are visible in the inside of the solid foam. Those regions are nearly inaccessible for the fluid flow.

The cuboid identification case is investigated for higher Reynolds numbers, where $Re = 10$ and 20 are computed for the fixed grid resolution of $N = 32$. Table 3 shows the computed quality measures regarding the different Reynolds numbers. Although there is a decreasing tendency in the Jaccard index for higher Reynolds numbers, the values are still very high with ≥ 0.93 as well as the number of correctly identified cells dominates the false predictions. As (15) shows, the sensitivity of the local control to the objective is proportional to the local velocity which is vanishingly small in the wake region downstream of the cuboid, leading to insensitivity. Analogous to above, Fig. 4 is used to translate the recovered permeability into the RVN for different Reynolds numbers. By comparing the permeability at the front side, different Reynolds numbers yield different reconstructed permeability values, i.e., $K_{Re=1} = 1.28 \times 10^{-5}\,\text{m}^2$ and $K_{Re=20} = 0.99 \times 10^{-5}\,\text{m}^2$. For all Reynolds numbers, the RVN yields again $\approx 1\%$, the same value as in the previous grid study showing that the RVN successfully shows (at least locally) the independence regarding the grid resolution and the Reynolds number.

6.2. Topology identification of a foam from simulation data

To test the applicability of the presented method on more complex geometries, the topology of an 10 pores per inch (PPI) Al2O3 OCF is reconstructed from simulation data. The input velocity distributions are simulated by using a STL (stereolithography) model which is created from CT scan images following the workflow of Sadeghi et al. [17]. A pipe wall is added to the OCF shown in Fig. 7b. The STL model is load in into the framework where an binary porosity distribution is computed either by a cell being inside or outside of the geometry. The resulting discrete reference porosity distribution in OpenLB is shown in Fig. 7c. Fig. 7b depicts inner cavity structures in the foam which are also visible in the computed reference porosity field in Fig. 7c. This porosity distribution is then used to simulate the reference velocity field via HLBM and is used as the input data for the optimization algorithm.

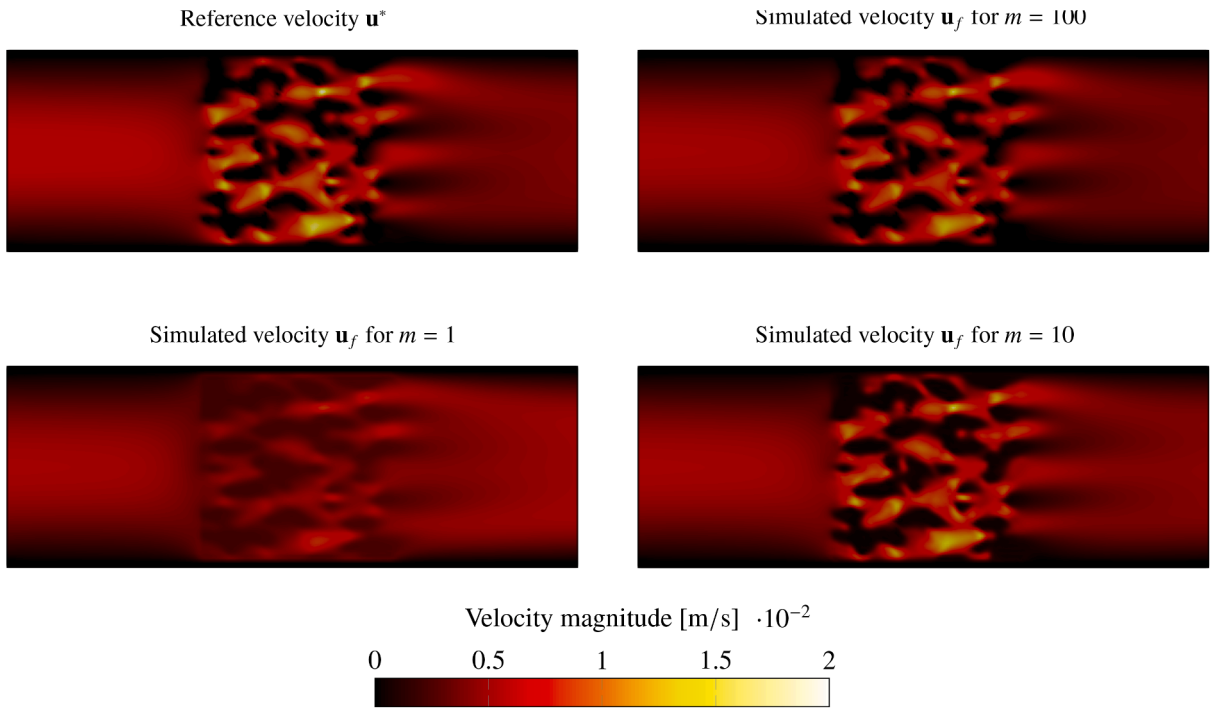

Fig. 8. Recovered velocity distributions in the x-z-plane during at various optimization steps in the OCF case. The reference velocity distribution is shown at the top left.

The set up for the simulations to compute the reference velocity distribution and the simulations performed during optimization are identical which allows to neglect discretization, boundary, model, and interpolation errors. This way the pure accuracy of the optimization algorithm can be investigated. The inflow and outflow length are chosen as $L_{\text{in}} = L_{\text{out}} = 24.5\text{mm}$, the length of the design domain as $L_{\Omega^\alpha} = 24\text{mm}$, and the diameter of the cylindrical shaped flow domain as $D = 25\text{mm}$. The diameter is resolved by $N_D = 80$ lattice cells resulting in a cell length of $\triangle x = 0.3125\text{mm}$. The Reynolds number is set to $Re = 100$ where it is computed as $Re = \bar{\mathbf{u}}_{\text{in}} D/\nu$ with $\bar{\mathbf{u}}_{\text{in}}$ being the average inflow velocity. By referring the characteristic length to the pore size, this 10 PPI foam results in an average pore size of 2.54mm. This results in a pore Reynolds number of $Re_P = 10.16$. The kinematic viscosity is chosen as for water leading in $\nu = 10^{-6}\text{m}^2/\text{s}$. This results in a LBM relaxation time is set to $\tau = 0.53\text{s}$ together with diffusive scaling for the time discretization. For the boundary conditions of the primal problem, the Poiseuille velocity profile is set at the inflow, a pressure is computed from the density with $\rho_{\text{out}} = 997\text{kg}/\text{m}^3$ via a pressure boundary, where the equilibrium boundary treatment is used. At the pipe walls a no-slip boundary condition is applied via bounce-back. In the dual simulation, the sensitivity of the objective regarding the flow variables are computed by the adjoint variable φ_i. As only Dirichlet-type boundary conditions are applied in the primal problem and by assuming negligible sensitivity from the boundaries as in [49], at all boundaries of the dual simulation the bounce-back method is applied as in [31]. That is, at the boundaries the state variables are not sensitive to the changes applied by the design, and thus set to zero. For the optimization, the initial guess is set to be a uniform distribution of $\alpha^0 = 2.908$, with the permeability of $K = 10^{-8}\,\text{m}^2$ resulting in a lattice porosity of $d = 0.948$. The reference domain is set equal to the flow domain.

Fig. 8 shows the comparison between the reference velocity distribution and the recovered velocity field by solving the inverse problem. The velocity fields at different stages during the optimization procedure are shown and it can be observed that beginning from a blurry velocity field, it is reconstructed by the presented method. Fig. 9 shows the comparison between the reference porosity distribution and the recovered porosity field by solving the inverse problem. Here, the separation of the low and high porosity values are illustrated for the same optimization steps as in the previous figure. For the optimization step 100, the majority of the porosity values are either close to zero or one, indicating a clear identification of solid and fluid cells. Fig. 10 illustrates the deviation in the recovered velocity and porosity distribution compared to the reference solution over the optimization procedure. It can be observed that for both the error is minimized over the iterations where in the last optimization step $m = 100$ the absolute error regarding the velocity is almost not visible compared to the initial optimization step. For the difference in the porosity distribution, even after 100 optimization steps several singular cells seems to deviate from the reference porosity with an absolute error of ≈ 1 which is the highest possible error. Those positions includes cells which are inside the inner cavities shown in Fig. 7c. This behavior is as expected as those cells inside of the solid structure do have negligible influence on the outer flow field.

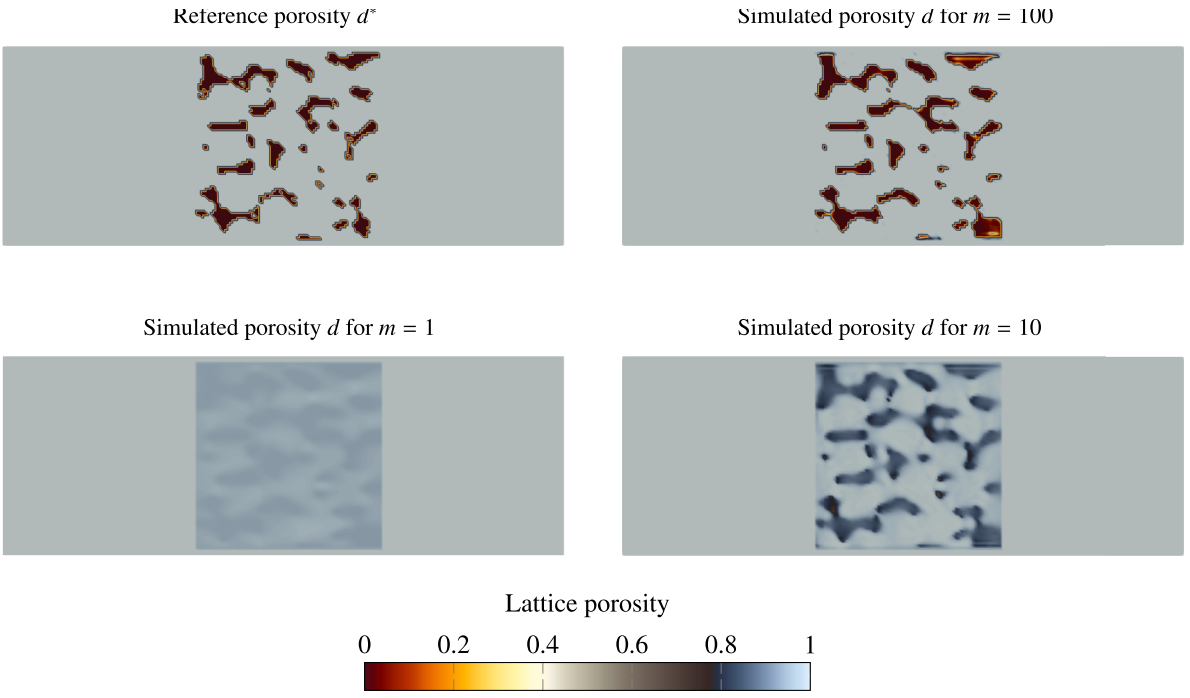

Fig. 9. Identfied lattice porosity distributions in the x-z-plane during at various optimization steps in the OCF case. The reference porosity distribution is shown at the top left.

Table 4
Quality measures of the identified OCF topology for various resolutions with $Re = 100$ ($Re_p = 10$). For the definition of the binary classification refer to Table 1.

N_D	Jaccard	P_T	TS	TF	FS	FF	B
80	0.834	0.83	74,882	272,547	14,480	684	0.989
133	0.783	0.43	334,415	1,280,847	82,274	10,496	0.980
164	0.774	0.54	619,420	2,430,571	160,691	20,260	0.976

6.2.1. Grid study

First, a grid study is conducted where the diameter resolutions $N_D = 80, 133, 164$ are simulated with a Reynolds number of 100. In this study, the resolution of the reference simulation and the simulations performed by the optimization framework is identical to exclude discretization and interpolation errors. Fig. 11a shows the relative velocity error over the optimization steps. The initial error of 80% is reduced to 10% in the first 20 optimization steps and is further reduced until 4% at 80 optimization steps. Afterwards only incremental decrease in the error is observable. Similar to the results in Section 6.1, the curve profile does align for the different resolutions indicating mesh independence of the recovered velocity field. The development of the Jaccard index over the optimization steps shows similar tendencies as in Section 6.1 where after 70 optimization steps only small improvements can be observed. This is interesting as the topology of the object seems to be not that significant regarding the optimization performance in number of required optimization steps. Rather does the resolution of the simulation as observed in the cuboid case and for the OCF, as in lower resolutions the increase in the Jaccard index in the first optimization steps is steeper. Fig. 11c shows the Jaccard index over the porosity threshold for the different grid resolutions. Again, we can observe different profiles of the curve for the different grid resolutions. However, in contrast to the cuboid identification case, the deviations are not significant as we do not observe the ambiguity issues in the inside of the foam as shown in Fig. 9. One explanation for this could be the low number of cell resolution regarding the foam strut structures ($\approx$ 8 - 12 cells at $N_D = 164$). Table 4 shows the computed quality measures in this grid study.

The Jaccard index slightly drops by increasing the resolution, which we expect is due to the inner cavities shown in Fig. 7c. This is also supported by the results shown in Fig. 10. Those cells are located inside of the geometry and have no influence on the outer flow field. By increasing the spatial resolution, more lattice cells are located inside the cavities resulting in the drop of the Jaccard index. The overall ratio of the binary classification results in similar values as well as the Bimodality index which yield very high values. This indicates the well separation of the fluid from solid cells as demonstrated in Fig. 9. Fig. 12 illustrates the recovered topology models which are produced as contour plots regarding the lattice porosity with $P_T = 0.9$. The geometry models can be compared with the reference geometry created from the CT scan images which is depicted on the left side. To emphasize the visual differences of the recovered models, in Fig. 12 lower resolutions of $N_D = 40$, 58, and 80 are computed. As the results show, the grid resolution

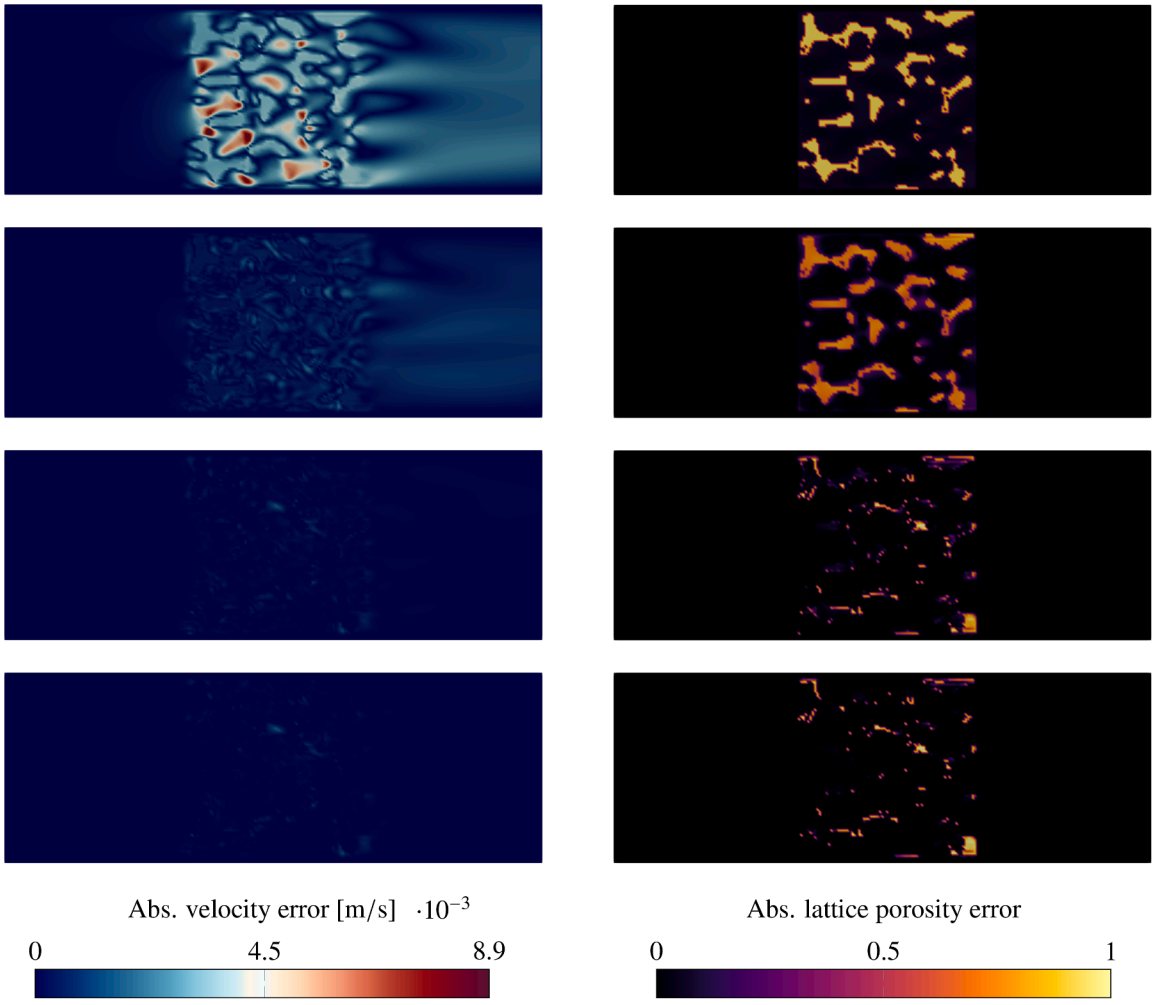

Fig. 10. Absolute error of the velocity magnitude distribution (left) and lattice porosity distribution (right) in the x-z-plane. From above, the error over the optimization steps at $m = 1, 10, 50, 100$ are shown.

is directly coupled with the resolution of the identified topology model meaning a more detailed reconstruction of finer structures requires a higher resolution.

6.2.2. Reynolds number influence

The generic case is studied for various Reynolds numbers to investigate the approach for different flow configurations. In the following, the results for $Re = 1$, 100, 300 are compared where the characteristic length is based on the pipe diameter. Using the average pore length instead, the pore Reynolds numbers of $Re_P = 0.1$, 10, 30, are obtained, respectively. Fig. 13 shows the development of the relative error regarding the velocity and the total derivative of the objective over the control. Therein, Fig. 13a shows that the final error is lower of decreasing Reynolds numbers, i.e., the error yield 1.5% for $Re = 1$ and 5.5% for $Re = 300$. Note, the logarithmic scale is applied on the y-axis to highlight the differences between the curves. Further, lower Reynolds numbers were tested but they did not showed major differences to the $Re = 1$ case and are thus omitted. Besides of observing the best results for the lowest Reynolds number, we can observe that for the two higher Reynolds numbers, the relative error in velocity does not show major decrease after the 80th optimization step. However, for $Re = 1$ is still a visible decrease on the relative velocity error visible which is why up to 300 optimization steps are computed where the gradients yield the same magnitude as shown in Fig. 13b. The gradients over the optimization steps also show the faster decrease for higher Reynolds number and reaching a state where further decrease in incremental, matching to the results on the left. Fig. 14 shows quality measures regarding the recovered geometry. Similar to the results in Fig. 13a, higher Jaccard index is obtained for the lower Reynolds number regime. Further, the index over porosity thresholds in Fig. 14b depicts larged deviation of the curves compared to the results in Section 6.2.1. The quality measures for the topology are listed in Table 5 together with the binary classification results in the final optimization step. The Jaccard index for $Re = 1$ yields 0.913 which shows the applicability of the presented method for complex geometries such as the OCF. Note, that due to the inner cavities shown in Fig. 7c there are already losses included in the Jaccard index. For comparison, with $Re = 300$ the Jaccard

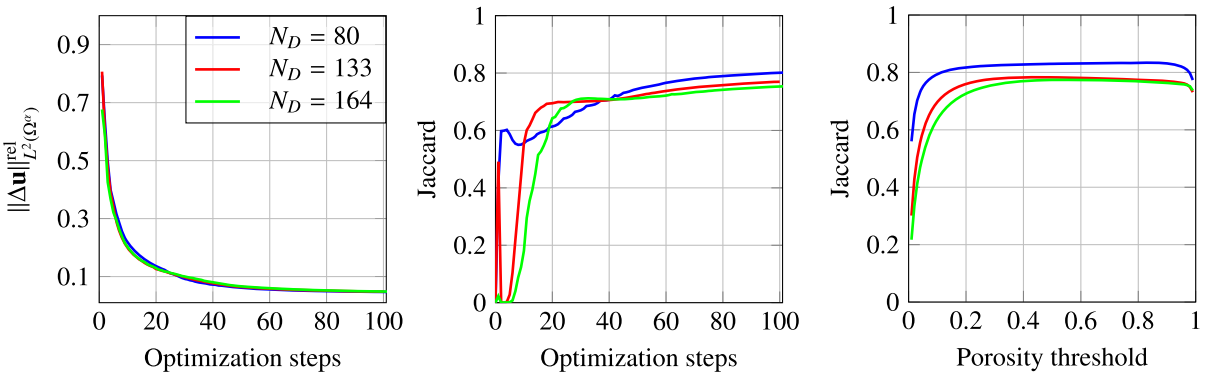

(a) Relative error velocity over optimization steps. (b) Jaccard index for $P_T = 0.9$ over optimization steps. (c) Jaccard index over porosity threshold P_T.

Fig. 11. Identical grid resolution for the reference simulation and the simulations performed by the optimization framework. Various grid resolutions are computed for the Reynolds number of $Re = 100$. Grid independence of the reconstructed velocity distribution is demonstrated. For the geometry only slight deviations of the curves are visible which are expected due to the inner cavities in the real OCF geometry.

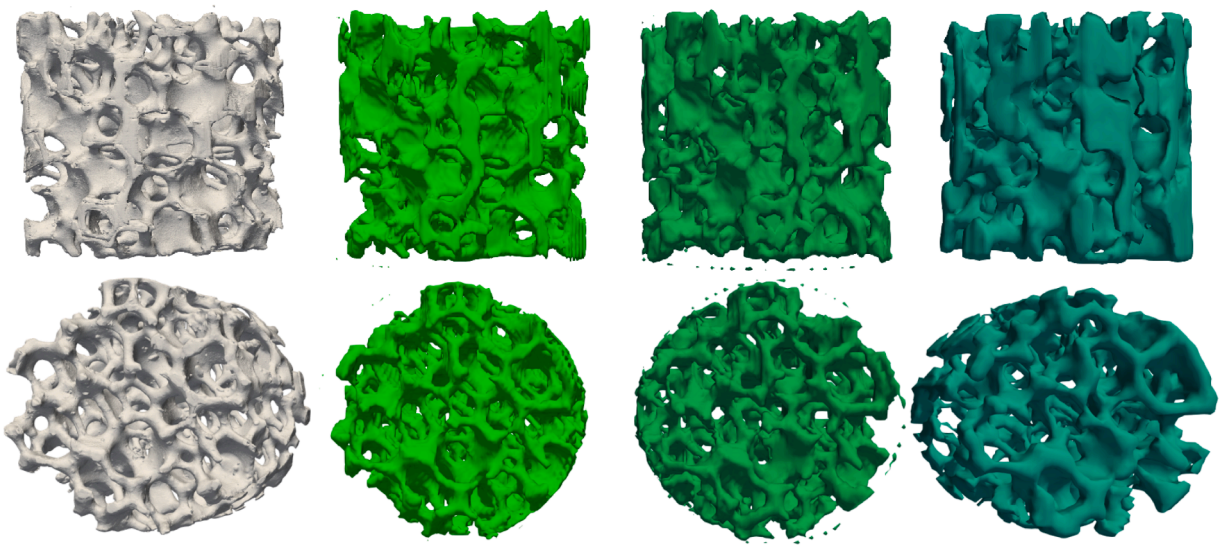

Fig. 12. Reconstructed topology models as a contour plot regarding the lattice porosity $P = 0.9$ for $Re = 100$. From the left: original STL model, $N_D = 80$, $N_D = 58$, $N_D = 40$.

Table 5
Quality measures of the identified OCF topology for various Reynolds numbers with $N_D = 80$. For the definition of binary classification refer to Table 1.

Re	Re_p	Jaccard	P_T	TS	TF	FS	FF	B
1	0.1	0.913	0.77	75,466	279,339	7673	115	0.982
100	10	0.835	0.85	74,825	272,829	14,183	756	0.989
300	30	0.798	0.91	68,844	276,325	13,493	3931	0.974

index yields 0.798 which is 12.5% lower then for $Re = 1$. The number of wrong predictions for both cases false solid and false fluid are significantly higher for higher Re shown in Table 5.

To gain a deeper understanding of the optimization algorithm, the porosity and permeability distributions are plotted as spectra over the optimization steps in Fig. 15. The entire interval for the porosity and permeability is divided into 100 equally sized sub-intervals where the number of cells in the corresponding sub-interval is counted and normalized over the total number of cells. This is done for all the cells inside the design domain. As the permeability tends to go towards infinity for the porosity approaching one, a limiter for the maximal permeability is computed from $P = 0.99$ such that all permeability values above are counted in the last interval. The spectrum of the reference porosity distribution which is computed from the STL model is consisting of only zero or ones leading in to a Bernoulli-distribution. Therefore, if the reconstructed spectrum is approaching such a distribution, it indicates a successful

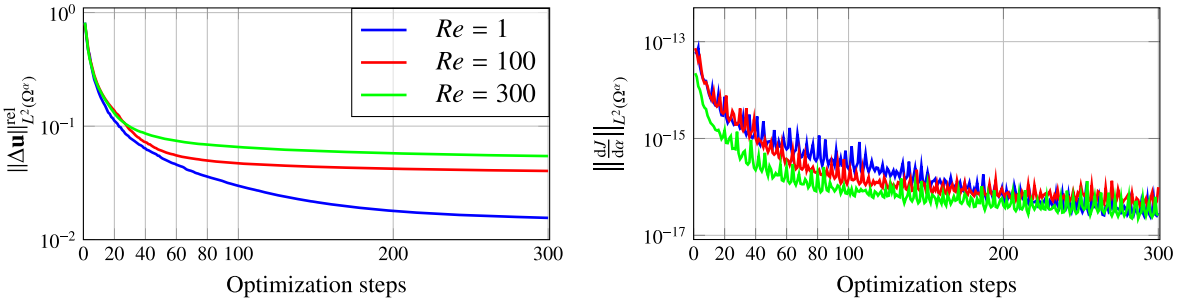

(a) Relative velocity error over optimization steps.

(b) L^2-norm regarding the total objective derivative over optimization steps.

Fig. 13. Comparison of the results for various Reynolds numbers for the OCF case. The quality measures for the reconstructed velocity distribution show an influence by the Reynolds number regarding accuracy and the optimization performance.

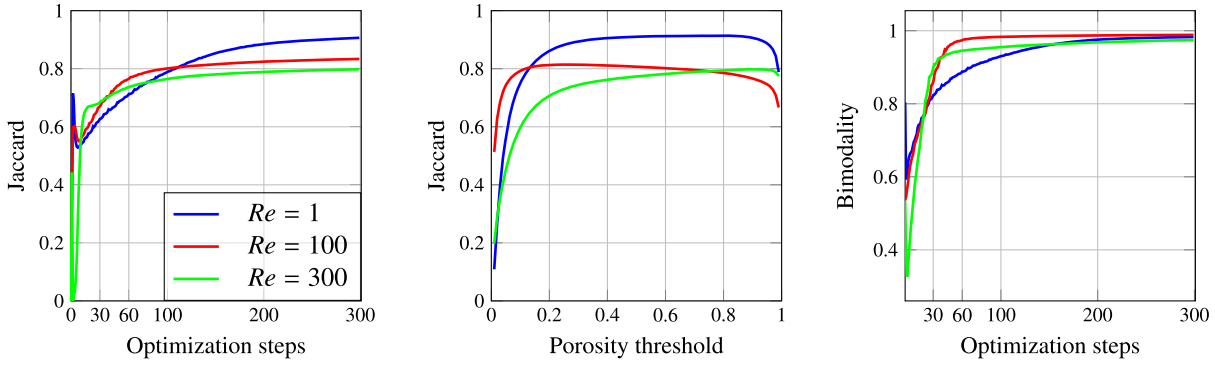

(a) Jaccard index over optimization steps.

(b) Jaccard index over porosity threshold.

(c) Bimodality coefficient over optimization steps.

Fig. 14. Comparison of the results for various Reynolds numbers for the OCF case. The quality measures for the reconstructed porosity distribution again show an influence by the Reynolds number regarding accuracy and the optimization performance.

topology identification. Fig. 15a and b shows first the homogeneous distribution of porosity and permeability at initialization where in the design domain the value of the initial guess is set. Over the optimization steps, it is shown that the distributions approaches a Bernoulli-distribution which is exactly expressed by the Bimodality index shown in Fig. 14c. Fig. 15c and d shows the lower region of the spectrum plot regarding the z-axis to visualize the immigration of the solid cells from the fluid cells identified by the optimization algorithm. In Fig 15c it is shown, that depending on the Reynolds number the intermediate porosity values are pushed faster in terms of optimization steps to $P = 0$ by the algorithm. That is, after 80 optimization steps the distribution for the higher two Reynolds numbers are quite close to a Bernoulli-distribution. For example, there are almost no visible differences for $Re = 300$ already after 60 iterations in the porosity distribution and the plot shows two clear peaks for the values zero and one showing a clear separation of the fluid and solid cells. However, for $Re = 1$ there are still a visible amount of intermediate porosity values at the 100th optimization step. That is, even after 100 optimization steps almost no cells reached a porosity value of zero. One reason for this behavior could be the Reynolds number dependency on the Darcy term as discussed in Section 5. The same permeability leads for increasing flow speed to a higher pressure drop over the cell and affecting on the velocity distribution. As the results of Fig. 4 shows, a lower permeability is required for higher Reynolds numbers such that a cell becomes "solid" from the flow perspective. Therefore, in the inverse problem the optimization algorithm requires a lower permeability value to imitate a solid cell. This explains the faster movement of the intermediate porosity values towards zero in the higher Reynolds number regime. The porosity spectrum supports the results shown in Fig. 14c where the Bimodality index is approximately at 0.9 at 100 optimization steps at $Re = 1$ and goes up to 0.99 for 300 optimization steps. This shows that reaching the quasi-steady state regarding the Bimodality index indicate a when to terminate the optimization procedure and the results are in an comparable state, e.g., here for the various Reynolds numbers.

The remaining question is the impact of the Reynolds number on the accuracy of the recovered velocity distribution and topology. The presented results in Figs. 13, 14, and Table 5 clearly shows better accuracy in the lower Reynolds number regime. To address this phenomena, the reconstructed velocity distribution in the x-z plane for $Re = 1$ on the left and for $Re = 300$ on the right is depicted in Fig. 16. The flow streams from left to right. The deviation of the recovered lattice porosity from the reference value is expressed via $\triangle P = P^* - P$ and is shown as a contour plot on top of the velocity field. That is, for $\triangle P > 0$, the optimization framework overestimated the solid geometry (FS case in Table 1) and for the case $\triangle P < 0$ the framework failed to recover the solid geometry at that position (FF case in Table 1). Already at the first glance, it is clear that there are less wrong predictions regarding the porosity in the lower Reynolds number case. However, in both figures the error in the lattice porosity occurs where the flow velocity is close

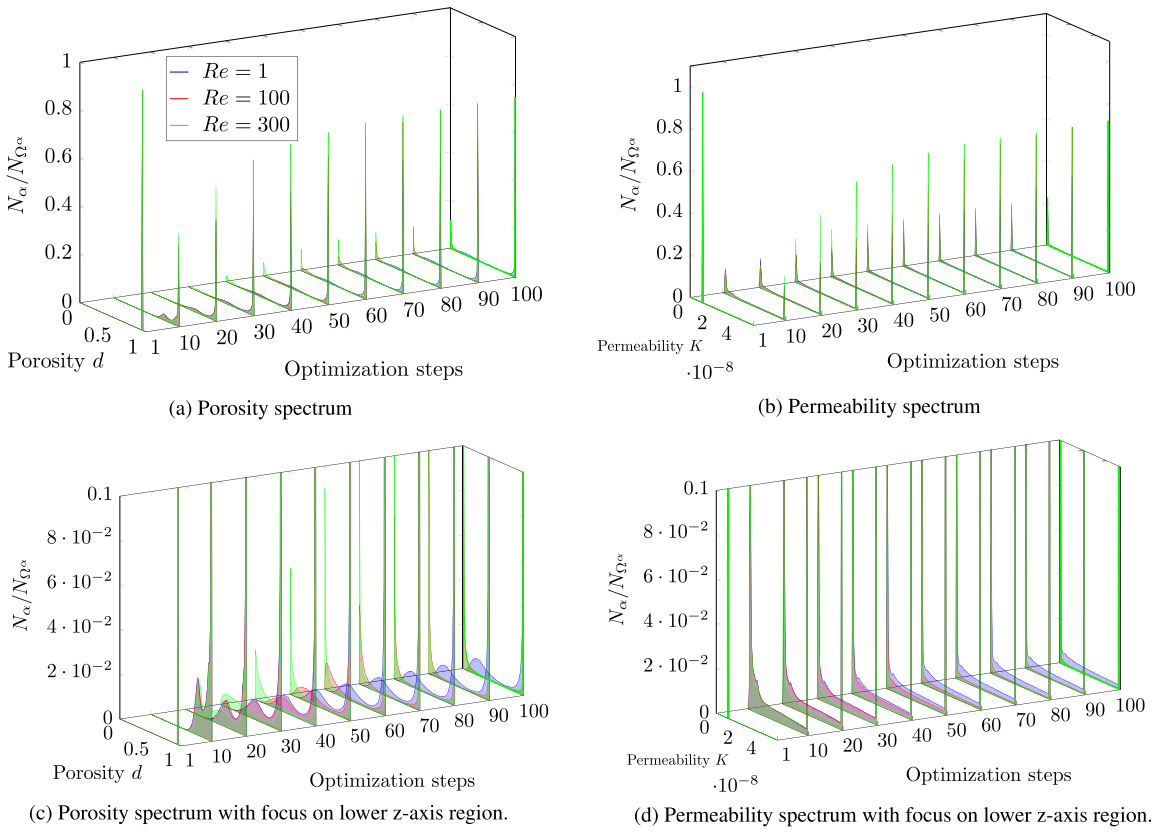

(a) Porosity spectrum

(b) Permeability spectrum

(c) Porosity spectrum with focus on lower z-axis region.

(d) Permeability spectrum with focus on lower z-axis region.

Fig. 15. Porosity spectrum over the optimization steps for various Reynolds numbers. In the left upper plot, the spectrum for all cells inside the design domains are illustrated, whereas in the right bottom the sec.

to zero. In the higher Reynolds number flow, there are larger stagnation points and wake regions, especially visible on the right edge of the foam in the right figure. This is the same ambiguity issue addressed in the cuboid identification case from Section 6.1. Additionally, the error caused by the inner cavities of the reference geometry is visible. Here, for both of the Reynolds numbers in Fig. 16, the overestimation of the solid geometry occurs much more frequently than the underestimation case. An explaining for this could be the resolution of the structures in the foam as stated already in Section 6.2. This leads to less insensible regions inside of the reconstructed geometry. The overestimation is mainly concentrated in the wake regions but small pores perpendicular to the flow direction and the boundary region of the geometry are prone regions to error. We conclude that the method is more suitable for applications at lower Reynolds numbers as the fluid flow conforms better to the geometry surface, leading in a better surface detection during the topology identification.

6.2.3. *Artificial noise*

Measurements generally contain noise signals, which motivates us to study impact of noise signals induced in the reference velocity field on the optimization results. For simplicity, the noise signal distribution is modeled as Gaussian with a zero mean and standard deviation of $\sigma \in \mathbb{R}$. The signal-to-noise ratio (SNR) quantifies the noise signal intensity, defined here as

$$\mathrm{SNR} = \frac{\mathrm{S}}{\delta}, \tag{23}$$

where S denotes the average noise-free signal intensity which is in our case the average velocity magnitude in the simulation domain. To cover a wide range of different SNR, investigations are conducted for the ratios $\mathrm{SNR} \in \{1, 3, 5, 10\}$. Fig. 17 depicts slices of the noised reference velocity field for various SNR in the x-y plane. This is used as the input for the optimization framework to reconstruct the velocity field and geometry model. The relative error over the optimization steps are depicted in Fig. 18a where the relative error is computed against the noise-free reference velocity distribution. The dashed lines shows the relative error which is purely caused by applying the noise signals on the reference data, i.e., $||\Delta\mathbf{u}||^{\mathrm{rel}}_{L^2(\Omega^\alpha)} = \sqrt{\Sigma_{\mathbf{x}\in\Omega^\alpha}(\mathbf{u}^* - \mathbf{u}^*_{\mathrm{noise}})^2 / \Sigma_{\mathbf{x}\in\Omega^\alpha}(\mathbf{u}^*)^2}$. For each investigated SNR, we can observe that our framework successfully reduces the relative error in the velocity field beyond the error induced by the noise signals. That is, for $\mathrm{SNR} = 5$ the noise signals induce an error of 50% while after the optimization the error is reduced to 14% showing the capability of noise reduction of the presented method. For the case $\mathrm{SNR} = 1$, Fig. 18b shows the comparison of the reference velocity with and without noise and the reconstructed velocity profile along the z-axis of the simulation. Therein, we can observe that the reconstructed velocity profile is smooth and shows even for this high noise signal intensity a similar profile as in the original

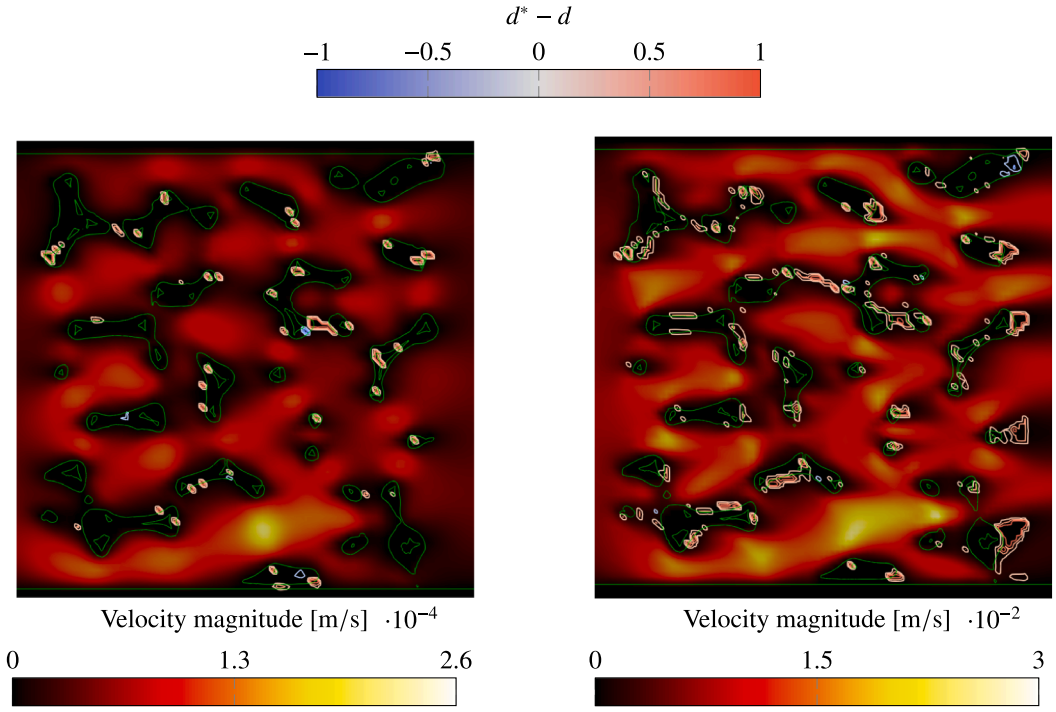

Fig. 16. Slices in the x-z-plane of the velocity distribution and the STL geometry (green contours) of the OCF. The signed deviation of the obtained lattice porosity from the reference solution is illustrated via contour plots on top of the slices where on the left $Re = 1$ and right $Re = 300$. The error prone regions are gathered where the flow velocity is near zero, i.e., stagnation, wake, and boundary regions. (For interpretation of the references to colour in this figure legend, the reader is referred to the web version of this article.)

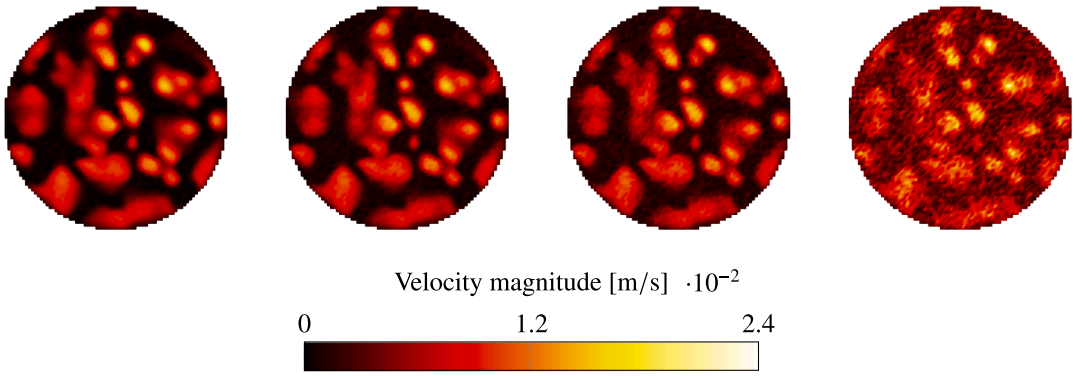

Fig. 17. Slices of the reference solution in the x-y-plane where artificial noise signals are induced. The intensity of the noise signals are varied here from the left: SNR = 10, 5, 3, 1.

reference data before applying the noise signals. SNR equal to 5 and 10 lead to deviation of the relative velocity error compared to the noise-free case less than 1% at optimization step 40. Shortly after, the optimization algorithm fails in finding a suitable step size and terminate. Fig. 19 depicts the reconstructed velocity and porosity field for the different SNR. In the velocity field with SNR = 1, we can observe small floating solid artifacts in the velocity field which were caused by the fractal structures in the porosity field. However, for all SNR the reconstructed velocity distribution looks smooth and show a successful noise reduction compared to the noisy reference velocity distribution shown in Fig. 17. In the reconstructed porosity field, the deviation of the optimization results are more visible. That is, for decreasing SNR the lattice porosity distribution gets more diffusive regarding the values, i.e., the increase of lattice porosity values far from zero or one. This shows the difficulty in separating the solid from the fluid cells which can be interpreted as a sort of ambiguity problem.

Table 6 lists the obtained quality measures of the recovered geometry. For SNR of 10, 5, 3, and 1 the respective decrease in the Jaccard index relative to the noise-free case is 5%, 8%, 16%, and 31%. The unclear classification of the lattice porosity values lead in the

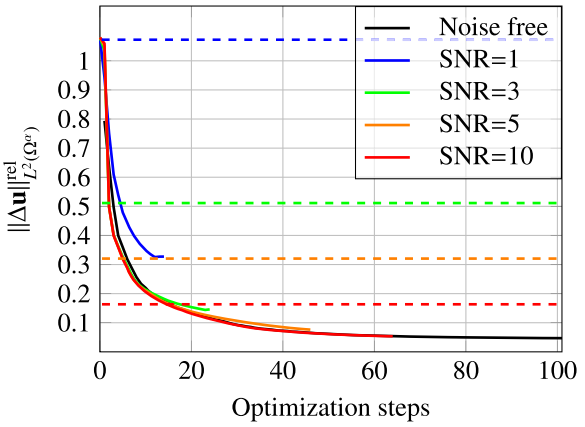

(a) Relative velocity error over optimization steps.

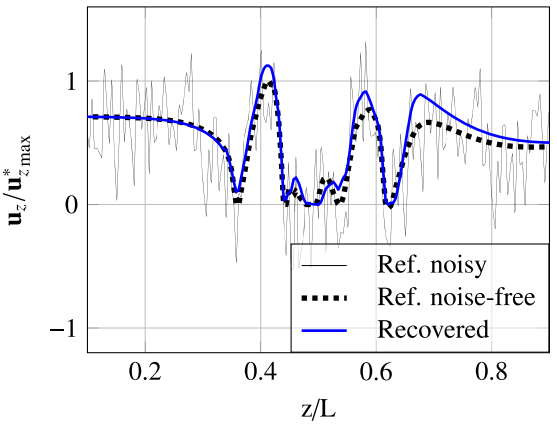

(b) Comparison of velocity profiles along center axis for SNR = 1.

Fig. 18. Obtained quality measures regarding the velocity distribution for various SNR with $Re = 100$ and $N_D = 80$. In the left figure, the dashed lines depict the error induced solely by the artificial noise signals. Successful noise reduction is demonstrated as the optimization framework reduces the initial error far beyond the dashed line as the relative velocity error is computed against the noise-free reference velocity. On the right the noise reduction is showed for the velocity profile along the z-axis.

Table 6
Quality measures of the identified OCF topology for various SNR at the final successful optimization step. For the noise-free case optimization step is $m = 100$.

SNR	Jaccard	Bimodality index
Noise-free	0.835	0.984
10	0.791	0.970
5	0.762	0.887
3	0.701	0.742
1	0.576	0.738

decrease of the Bimodality index. Analogous to Section 6.2.2, the found porosity spectrum in the final optimization step is visualized for various SNR in Fig. 20. Fig. 20a illustrates the whole spectrum and shows at $P = 0$ and 1 the decrease in number compared to the noise-free case. By further lowering the SNR, the clarity of a cell being solid or fluid becomes more diffusive, resulting in a distribution as shown in Fig. 20b. It shows that for a SNR of less than 5 there are almost no cells being identified as clearly solid in terms of the lattice porosity equal to zero. One reason for this diffusive distribution could be the early termination of the optimization problem, as the porosity distribution shown in Fig. 20b shows similarities to the distributions in Fig. 15c for the corresponding optimization steps. That is, due to the induction of artificial noise signals, the algorithm struggles to find a lower objective value leading in a high number of attempts to find a suitable step length. This point differs from the faced ambiguity issues in the previous sections where the optimization framework has difficulties in finding an clear solution regarding the lattice porosity.

Fig. 21 shows the reconstructed geometry models as contour plots for a lattice porosity threshold of $P = 0.9$. While the foam structure is clearly recognizable, for the models with lower SNR, a post-processing might become necessary in order to remove single fractals which are in the bulk of the fluid.

6.3. Topology recovery of a porous foam from MRV data

Finally, 3D MRV data is used as the input for the inverse problem to reconstruct the foam topology as well as in attempting to reduce the noise in the flow distribution. The experimental set-up for the MRV measurements consists of an 10 PPI Al2O3 OCF placed in a glass reactor (diameter 25 mm). Sealing tape is wrapped around the outside of the OCF to prevent bypass flow and fix it's position. Additional OCFs are added in front of and behind the sample to ensure Poiseuille-profiles to match the numerical boundary conditions. A constant volumetric flow of water (200 mL/min) thorough the glass reactor is ensured using a centrifugal pump (DC 15/5, HARTON Anlagentechnik, Alsdorf, Germany) and a Coriolis mass flow meter and control valve (mini CORI-FLOW M12V14I, Bronkhorst, Karmen, Germany). The MRV measurements are performed using a 7T MRI scanner (BioSpec 70/20 USR, Bruker BioSpin MRI, Ettlingen, Germany) equipped with a horizontal 72-mm bore birdcage 1H quadrature transceiver RF coil (Bruker BioSpin MRI, Ettlingen, Germany). For flow detection, a dual-$VENC$ phase-contrast (PC) spin-echo (SE) pulse sequence is used as described in earlier works [21]. Frequency encoding (50 kHz sweep width) in $Read$-direction parallel and two $Phase1, 2$ encoding perpendicular to flow direction were used for spatial imaging. A resolution of $40 \times 40 \times 80$ in a FOV of $36 \times 36 \times 36$ mm, corresponding to an in-

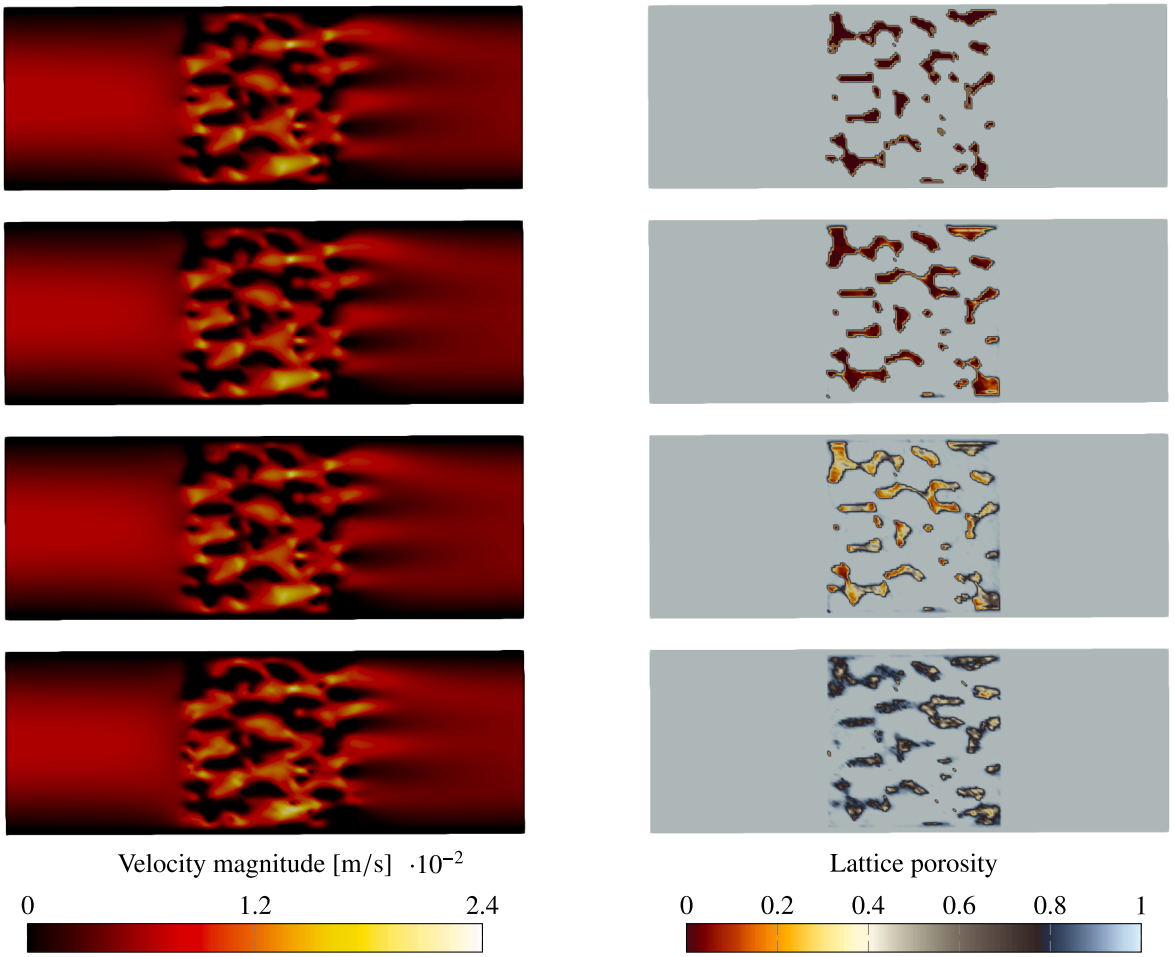

Fig. 19. Reconstructed velocity and lattice porosity distribution shown in the x-z-plane for various SNR listed from top: Noise-free reference solution, SNR 10, SNR 5, SNR 1.

plane resolution of 0.9 mm with an resolution in the through-plane direction of 0.45 mm is used. In between the 2π-Pulses distanced by $TE = 6$ ms, velocity encoding is applied using bipolar velocity encoding gradient pulses G_v and $-G_v$ of duration $\delta = 800\,\mu$s and distance $\Delta = 2$ ms. Depending on the gradient amplitude used, a maximum velocity for aliasing-free detection $VENC = \pi/\Delta(G_v\delta)^2$ can be resolved. For this pulse sequence, $VENC_1 = 0.045$ m/s and $VENC_2 = 0.02$ m/s are combined to combine the velocity range and sensitivity of both $VENC$s respectively. To fully capture the three-dimensional velocity field, a 4-step Hadamard encoding scheme is used. Overall, the pulse sequence repeats all 4 velocity encoding steps with both $VENC$s two times at even and uneven echoes, amounting to $TR = 3$ s for the 16-echo pulse sequence. The overall scan time is 5.3 h. The SNR of the MRV measurements is evaluated following established procedures from the literature and yielded a value of 74.4455. This corresponds to an estimated velocity uncertainty of $1.7103 \times 10 - -4$ m/s. Raw data processing was performed using in-house developed MATLAB[2] scripts. This includes first an image Reconstruction of frequency- and phase encoded raw data, then a velocity decoding according to Hadamard-encoding scheme, followed by a combination of $VENC$ 1, 2-images to correct aliasing artifacts. Finally, a velocity offset correction using an zero-flow measurement is applied. After the processing the MRV data is exported to the VTI data-format of the VTK library.[3] In OpenLB the velocity distribution from the MRV measurement is sampled onto the simulation grid points and are compared against the simulated velocity field. The spatial resolution of the simulation grid is chosen to be equal as in the MRV measurements leading to the same grid size of $\triangle x = 0.45$ mm and the diameter of the foam resolved by 51 cells. To assess the influence of the numerical resolution, an additional reconstruction based on simulation data as in Section 6.2 was performed on a coarser grid (resolved by 40 cells). The final deviation remained below 4%, indicating that the chosen discretization is sufficiently fine for the present study. The volume flux and viscosity from the experimental setup results in a Reynolds number of 170. For the kinematic viscosity of water at room temperature, $\nu = 1 \times 10^{-6}\mathrm{m}^2/s$ is set. In order to match the experimental inflow conditions, Poiseuille flow profile is prescribed.

[2] MATLAB R2019a, The MathWorks, USA, https://www.mathworks.com/.
[3] VTK - The Visualization Toolkit 9.3., Kitware, USA, https://vtk.org/.

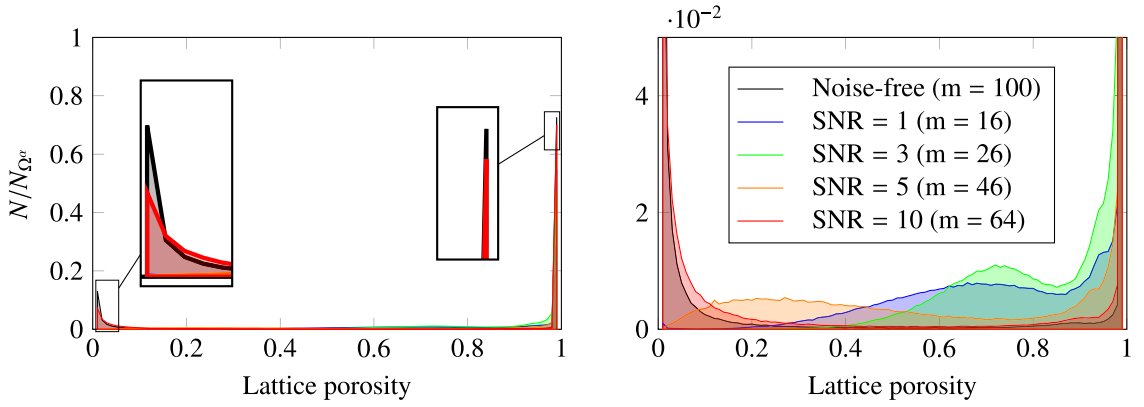

(a) Porosity spectrum for various SNR. The last successful optimization steps has been compared.

(b) Porosity spectrum in the lower region for various SNR. The last successful optimization steps has been compared.

Fig. 20. Porosity spectrum for various SNR with $Re = 100$ and $N_D = 80$. The counted cell number is normalized over the total number of cells in the design domain. On the left the whole spectrum is shown, where the number of cells with a porosity of zero and one decreases for SNR = 10. On the right the lower region of the spectrum is shown, where for lower SNR the reconstructed porosity distribution becomes more diffusive and almost no values reaches a zero porosity.

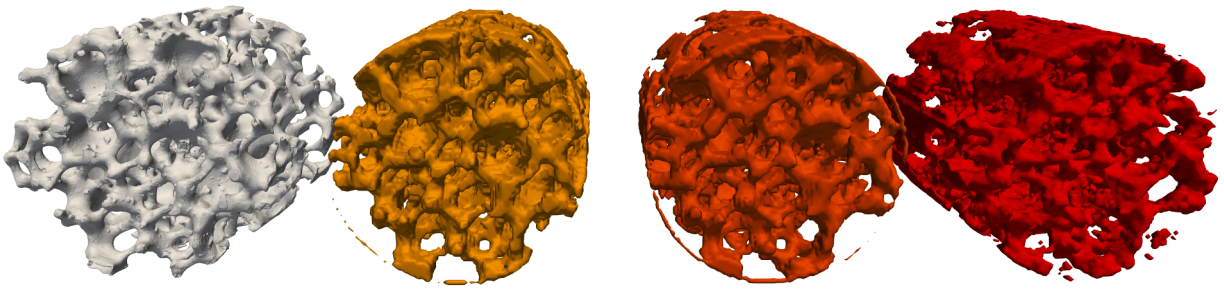

Fig. 21. Reconstructed topology models as contour plot regarding the lattice porosity $P = 0.9$ for $N_D = 80$ and $Re = 100$. From the left: original STL, SNR = 10, SNR = 5, SNR = 1.

However, due to stability issues a larger inflow length of $L_{\text{in}} = 100mm$ has been employed. All of the remaining simulation and optimization parameters as well as boundary conditions are chosen identically as in the previous cases in Section 6.2.

With the measurements obtained with MRI, we now have three different data sets for the velocity distribution and the geometry, respectively. First, we treat the CT-scan-based STL model (CT) as the ground truth regarding the geometry and the simulated velocity distribution using that STL model (CT-CFD) as the ground truth regarding the velocity distribution. Then, we have now the measured MRV data set (MRV) with a geometry model which is created by segmentation of the signal amplitude image (MRI). Finally, through our presented method the reconstructed flow domain geometry and the velocity distribution is obtained (CFD-MRI). As the MRV measurements and the CT-scan imaging are performed at different institutions, the matching of the translation and rotation of the datasets is necessary. The two datasets are aligned based on the velocity fields CT-CFD and MRV using MATLAB to maximize the normalized cross-correlation of each image slice as in earlier works [17,21]. Compared to the investigations in Section 6.2, we now introduce a variety of error sources into the problem, i.e., boundary effects, discretization errors, noise signals from MRV measurements, errors due to displacement, etc.

Fig. 22 shows the comparison of the velocity distribution and the geometry in the x-z-plane for the three data sets. To create a binary geometry distribution for the signal amplitude image and the reconstructed geometry via CFD-MRI, the Otsu's method [56] and a porosity threshold of $P_T = 0.97$ has been used, respectively. While visually the velocity distributions shows similarity, the geometry distribution obtained via MRI present larger strut structures compared to the other two data sets which is likely due to the partial volume effect [57]. In the reconstructed geometry via CFD-MRI, the overestimation of the geometry model can be suppressed as shown in Fig. 22. In Fig. 23a, the relative velocity error between the three velocity distributions CFD-MRI, MRV, and CT-CFD are plotted over the optimization steps. The blue line is proportional to the objective value which can be seen being reduced successfully over the optimization steps. Before performing CFD-MRI, the error between MRV and CT-CFD (ground truth) has been assessed and visualized as the black solid line in Fig. 23a with 43% relative error. Solving the inverse flow problem, leads to a reduce in the error to CT-CFD (purple line) to 38% which corresponds in an improvement of 11.6%. Regarding the Jaccard index, the reconstructed geometry via CFD-MRI yielded 0.46 for $P_T = 0.97$ which is a 12% increase compared to the Jaccard index between MRI and the CT-scan model with 0.41 as shown in Fig. 23b. As for the computation of the Jaccard index the binarization of the geometry distributions is necessary, in

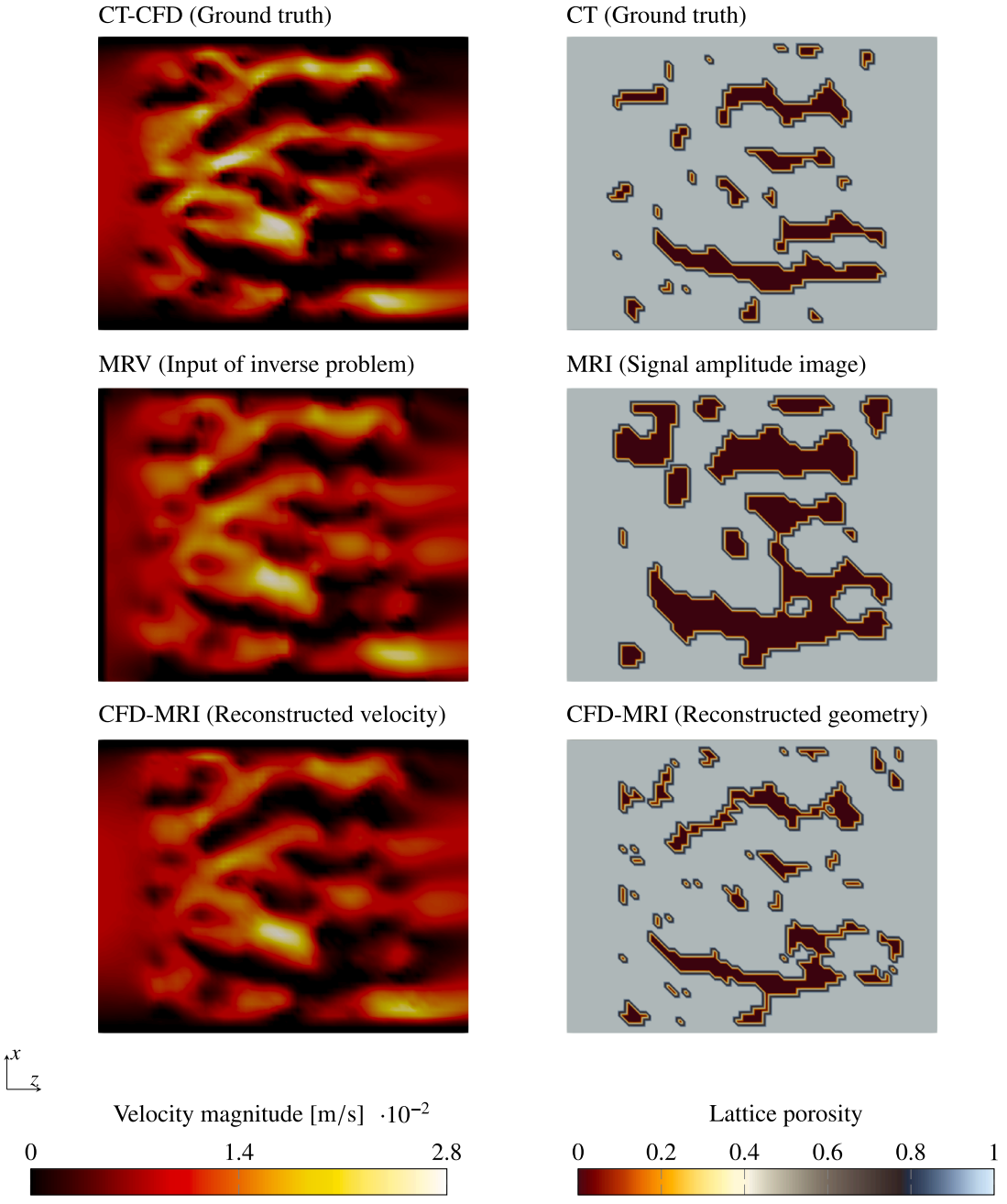

Fig. 22. Comparison of the velocity and geometry in the x-z-plane for all three data sets.

addition the PPC is compared as this index allows the computation of the correlation of two non-binary distributions. Fig. 23c shows the PPC over the optimization steps where the black solid line presents the index before applying CFD-MRI leading in a correlation of 0.5 between the ground truth and MRI. After 30 optimization steps the PPC gradually increases and reaches the correlation of 0.514 after 100 optimization steps which presents a slight increase of 2.8%. The extracted surface models are visualized in Fig. 24.

7. Discussion

In this Chapter, the answers to the formulated research questions in Section 1 are given.

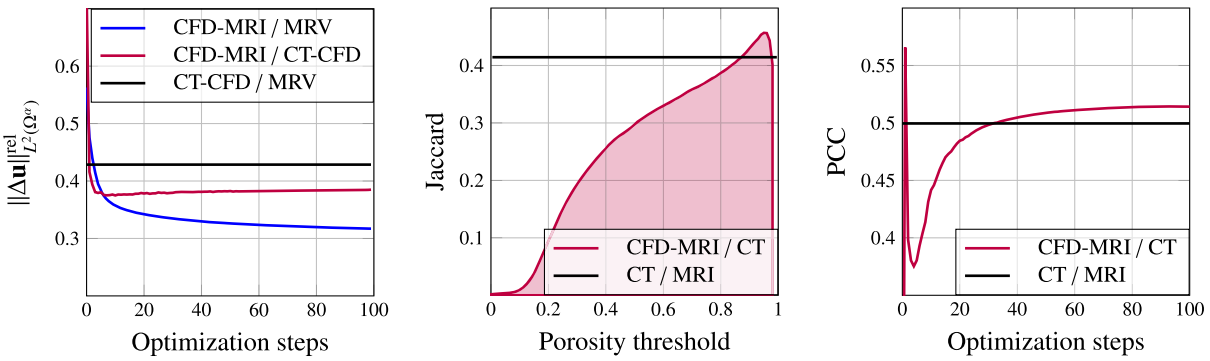

(a) Relative velocity error over optimization steps. (b) Jaccard index over porosity threshold. (c) PPC over optimization steps.

Fig. 23. Quality measures regarding the reconstructed velocity and geometry for using measured MRV data as input for the inverse problem. The mid plot is presenting the Jaccard index computed using the results at the final optimization step ($m = 100$).

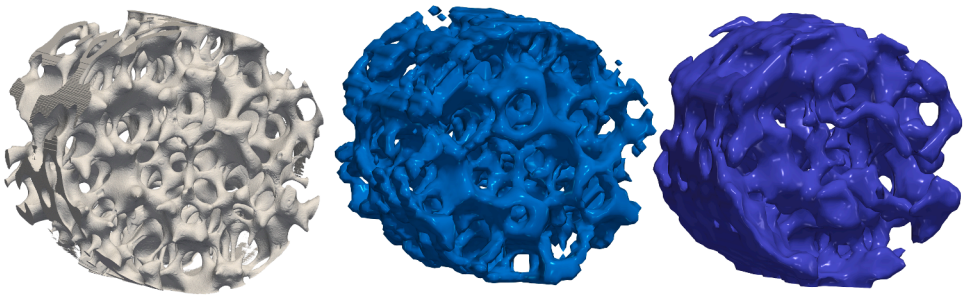

Fig. 24. Comparison of extracted surfaces. From the left: CT-scan model, Porosity level surface from CFD-MRI, signal amplitude level surface obtained from MRI.

How does the framework react to different flow configurations regarding accuracy, performance, and robustness?

Accuracy:

Regarding the accuracy of the presented method, a huge impact has been shown by the Reynolds number. For the lowest Reynolds number of $Re = 1$, both the cuboid and the OCF yield higher accuracy regarding the relative velocity error and the Jaccard index. That is, the lower Reynolds number leads to smaller stagnation and wake regions in the flow of near zero velocity where ambiguity issues caused errors in the optimization results. Due to the inner cavities in the OCF, the higher resolution increased the number of grid nodes inside the cavities which are enclosed by the solid foam struts. These regions do have negligible influence on the outer flow field, resulting in overestimation of the solid object. In the cuboid case the inner cells showed higher porosity values than in the reference geometry which poses again ambiguity issues regarding the identified object. That is, the accuracy of the results is mainly dependent on the presence of ambiguity where a low Reynolds number is the choice to reduce those issues. By inducing artificial noise signals in Section 6.2.3, for too low SNR, the optimization framework terminated at an earlier number of iterations as it fails to find a suitable step size. However, the reduction in the relative velocity error showed great capabilities in noise reduction of the proposed framework. In contrast, the Jaccard index suffers from the early termination, leading to diffuse values of the recovered lattice porosity across the interval, making it a challenging task to find a suitable value for the porosity threshold to compute the index.

Performance:

The performance of the framework can be separated into two types, the performance regarding the reduction of the objective over the conducted optimization steps and the computational performance. The latter will be addressed only briefly as this is not the main focus of the current work. The first 10 to 20 optimization steps include the majority of the reduction regarding the objective value. This shows the great convergence rate of the L-BFGS algorithm together with the applied step control. Comparison to different solvers like the steepest descent method has been not conducted as this has not been the focus of this work. Regarding the development of the Jaccard index over the optimization steps, similar tendencies as for the velocity has been observed. The first few steps resulted in a rapid increase in the index. While after $\approx 50 - 60$ optimization steps the relative velocity error only decreased incrementally, for the Jaccard index it takes slightly more number of iterations ($\approx 60 - 70$) until a quasi-steady development is observed. Interestingly, by increasing grid resolution, the number of iterations required during the steep increase in the Jaccard index at the beginning increased while afterwards no significant differences could be observed. In the OCF, the increased Reynolds number showed faster convergence

of the optimization results. That is, the impact of the Reynolds number on the permeability as shown in Section 5 lead to a higher sensitivity of the permeability on the velocity distribution.

For the computational performance, a significant improvement has been observed by the use of GPUs instead of CPU only simulation. Due to the iterative nature of the optimization framework, the speed-up of the primal and dual simulation greatly enhances the overall performance of the method. To further improve the computation speed, CSE on the collision kernels and compiler optimization are utilized. This way, we could perform all computations locally, solving distributed control problems with a total number of cells of 15×10^6 and 3×10^6 control variables corresponding to the number of degrees of freedom in our optimization problem. Solving this problem takes a reasonable time of ≈ 20 h for 100 optimization steps consisting of in total 200 simulations with 100 primal and adjoint simulations each. Therein, the adjoint simulation took a comparable time as the forward simulation, matching to findings in the literature [58]. Tasting the scalability of the presented framework on high performance computing clusters are planned in the future. The termination due to convergence in the adjoint simulation contributes also a significant amount to the reduction of the computational time as stated in [46].

Robustness:

Regarding the robustness of the framework, two aspects can be reported which are about the choice of the initial guess regarding the permeability and stability of the primal and dual simulations. The former has been observed to be not relevant in the cuboid case, as initial guesses in the interval of $[10^{-8}, 10^{-2}]\mathrm{m}^2$ lead to the identical results for the identified topology, except for regions where ambiguity issues occur. In the OCF case a high permeability needed to be set for the initial guess as the design domain filled the whole diameter of the pipe geometry.

Almost no stability issues are observed in the primal problem, while the dual problem showed sensible behavior for higher Reynolds numbers. One approach to tackle this issue is to lower the relaxation time to increase the time discretization or to simply increase the spatial resolution. Another factor played the inflow length as in the dual simulation the sensibilities propagate towards the inflow due to the negative sign in the propagation term in (13). As Dirichlet-type boundary conditions are applied at the inflow, the corresponding boundary treatment of bounce-back in the dual problem is applied to force an insensibility of the inflow velocity by the control variables. However, if the boundary length is too short, high gradients in the inflow region occur in the dual simulation leading to instabilities.

Is this method feasible to recover complex shapes like the OCF (using simulation data as input)?

Yes, a similarity index of 0.913 could be obtained in the OCF case despite the insensitive inner cavities in the original geometry. The identified geometry results in a relative velocity error of 1.5% compared to the input velocity distribution. Even for other flow configurations, as for higher Reynolds numbers $Re = 100$ and $Re = 300$, the framework recovered the geometry with similarity index of 0.835 and 0.798, respectively. When noise signals of SNR $= 10$ or SNR $= 5$ are introduced on the input data, the presented method still could recover the geometry with a loss in quality of only 5.3% and 8.7%, respectively.

What are the limitations/restrictions?

One main challenge to the topology identification problem pose the occurrence of ambiguity issues in the regions with near zero velocity, i.e., inside of an obstacle, boundary layers, stagnation, and wake regions in the flow. Ambiguity is enhanced by higher the Reynolds numbers as stagnation and wake regions in the flow field becomes more present leading to overestimation of solid geometry. Depending on the "thickness" of the geometry, ambiguity issues occur in the inside of the geometry in form of underestimation of the solid geometry as those region do not have an influence on the flow field which is thus not sensible for the optimization framework. Summarizing, regions with near-zero velocity are in general not sensible to the optimization framework and are therefore prone to ambiguity issues. That is, the relative error in the reconstructed velocity field only slightly drops but more significant losses in the Jaccard index are observed. In addition, the choice of the porosity threshold in order to compute the Jaccard index becomes more challenging when ambiguity issues becomes dominant. Another challenge occurs when noise signals are induced onto the flow field as discussed above. A promising approach to address the two limitations here could be to introduce regularization or penalization terms to counteract the ill-posed problem.

One remaining challenge presents the suitable choice of the porosity threshold required to compute the Jaccard index. In real application cases the true geometry is unknown such that a "look-up" of the threshold leading to the best Jaccard index is not possible. In the cuboid case first attempts in constructing a grid and Reynolds number independent indicator has been introduced, namely the RVN but it is still target of research. The discussed aspects in Section 5 in combination with the currently occurring ambiguity issues makes it to a very challenging task to construct an universal and robust method in finding the porosity threshold. Before starting with the numerical experiments solving flow domain identification problems, the impact of the grid resolution and Reynolds number on the lattice porosity/permeability is discussed in Section 5. Therein, the RVN is introduced to measure the impact of a local permeability on the flow field and it has been shown that the Reynolds number indeed has an influence on the reconstructed permeability distribution. A general method to determine the optimal lattice porosity threshold to compute the Jaccard index, i.e., the optimal choice of the threshold to obtain the best result geometry for the flow domain still is target of future research.

Finally, the limitation of the present approach to steady flows is briefly discussed. This limitation mainly arises from the adjoint-based gradient computation, since unsteady simulations require storage of the full primal solution trajectory for all time steps, resulting in substantially increased memory requirements. In addition, the treatment of unsteady flows increases both the complexity and the acquisition time of MRV measurements. However, with respect to the primary objective of the present work, namely the

reconstruction of geometry from flow-field information, this limitation is not considered critical, since steady laminar flow conditions can generally be established experimentally for the investigated class of problems.

How does the method perform when experimental MRV data are fed to the framework?

The presented method CFD-MRI archive an improvement in the velocity distribution and reconstructed geometry model compared to the input data set (MRV/MRI). That is, the CFD-MRI results showed less deviation to our ground truth data set (CT-CFD/CT) with 11.6% and 12% improvement regarding the flow distribution and the geometry, respectively. By comparing the results with those from Section 6.2, we can observe that the window of porosity thresholds regarding the Jaccard gets narrower when experimental data are used in order to get good results. Thus, the choice of the porosity threshold is crucial for an accurate geometry extraction. This can be also observed in the results obtained regarding the PCC which presented less improvement by CFD-MRI as the PPC operates on the non-binarized distributions. It is important to note, that the results presented in this study contains only preliminary insights as the parameter study on the MRI-side are planned in a future publication. Thus, the results shown here should be seen as *a-proof-of-concept* of the CFD-MRI method and are not meant to give an estimation of the possibilities of this approach.

8. Conclusion

In the presented manuscript the optimization framework combining adjoint lattice Boltzmann method with gradient-based optimization method is used to reconstruct the topology of an object from velocity distributions. First, the impact of the Reynolds number and grid resolution on the cuboid identification problem is investigated. Then, for a more complex application case, the reconstruction of the OCF has been conducted where first simulation data are used as input for the optimization algorithm. This validation set up provides a flexible environment to test the method as well as allows to neglect several error sources such as discretization, model, boundary, and measurement errors. Therein, an extensive investigation is conducted to investigate the influence of the Reynolds number, grid resolution, and noise signals on accuracy, performance, and robustness. Finally, real 3D MRV measurement data has been used for the reconstruction of the open cell foam geometry and evaluated regarding recovered geometry and velocity distribution. The results obtained from the CFD simulation using CT-scans of the OCF are used as ground truth to validate the output of the optimization framework where MRV data has been used. Findings has been thoroughly discussed in the discussion section by giving answers to the formulated research questions. A brief summary of the highlights of the presented work are as follows:

- Complex topology of an OCF is identified from simulation data with a relative velocity error of 1.5% and a Jaccard index of 0.913.
- The quality of the recovered OCF geometry is higher for lower Reynolds numbers ($Re \leq 1$) but the geometry is identified faster for higher Reynolds numbers, i.e., at $Re = 300$ the framework requires five times less optimization cycles.
- The development of the optimization objective is grid-independent. The ambiguity issues are however, grid dependent. That is, if the solid object contains too many grid cells over the thickness, ambiguity issues arise in the inside.
- The denoising capabilities of velocity distributions as presented in [46] could be confirmed by reducing 36% of the error produced by noise via optimization for the input data with a SNR $= 5$.
- CFD-MRI improved the quality of MRV/MRI measurements by reducing the deviation to our ground truth data set CT-CFD/CT with 11.6% and 12% improvement regarding the flow distribution and the geometry, respectively.

The advantages and possibilities of the presented novel approach in obtaining geometry models for numerical studies motivates for continuing the study in future works. Therein, we aim to apply regularization/penalization techniques to address the main challenges of ambiguity issues. Furthermore, as the results highly depend on the input data set, a follow-up work on identifying the feasible parameter regimes on the MRV side is in planned.

CRediT authorship contribution statement

Shota Ito: Writing – original draft, Validation, Software, Methodology, Investigation, Formal analysis, Data curation, Conceptualization; **Alexander Zimmermann:** Writing – review & editing, Software, Investigation, Data curation, Conceptualization; **Julius Jeßberger:** Writing – review & editing, Software, Formal analysis, Conceptualization; **Stephan Simonis:** Writing – review & editing, Formal analysis; **Adrian Kummerländer:** Writing – review & editing, Software; **Fedor Bukreev:** Writing – review & editing; **Jorg Thöming:** Writing – review & editing, Funding acquisition; **Georg Pesch:** Writing – review & editing, Funding acquisition; **Mathias J. Krause:** Writing – review & editing, Supervision, Software, Resources, Funding acquisition, Conceptualization.

Funding

This research was funded by the German Research Foundation for the project “CFD-MRI Reactions - A Combined Measurement-Simulation Approach for Reactive Flow Characterization”, grant number 517581625. .

Declaration of competing interest

The authors declare that they have no competing interests.

Acknowledgment

This work was performed on the HoreKa supercomputer funded by the Ministry of Science, Research and the Arts Baden-Württemberg and by the Federal Ministry of Education and Research. The authors acknowledge support by the state of Baden-Württemberg through bwHPC.

Data availability

Data will be made available on request.

References

[1] I. Fechete, Y. Wang, J.C. Védrine, The past, present and future of heterogeneous catalysis, Catal. Today 189 (1) (2012) 2–27. Catalytic Materials for Energy: Past, Present and Future, https://doi.org/10.1016/j.cattod.2012.04.003
[2] F. Lucci, A. Della Torre, G. Montenegro, P. Dimopoulos Eggenschwiler, On the catalytic performance of open cell structures versus honeycombs, Chem. Eng. J. 264 (2015) 514–521. https://doi.org/10.1016/j.cej.2014.11.080
[3] W. Zhu, N. Blal, S. Cunsolo, D. Baillis, Effective elastic properties of periodic irregular open-cell foams, Int. J. Solids Struct. 143 (2018) 155–166. https://doi.org/10.1016/j.ijsolstr.2018.03.003
[4] M. Bracconi, M. Ambrosetti, O. Okafor, V. Sans, X. Zhang, X. Ou, C.P. Da Fonte, X. Fan, M. Maestri, G. Groppi, E. Tronconi, Investigation of pressure drop in 3D replicated open-cell foams: coupling CFD with experimental data on additively manufactured foams, Chem. Eng. J. 377 (2019) 120123. https://doi.org/10.1016/j.cej.2018.10.060
[5] A. Della Torre, G. Montenegro, G.R. Tabor, M.L. Wears, CFD characterization of flow regimes inside open cell foam substrates, Int. J. Heat Fluid Flow 50 (2014) 72–82. https://doi.org/10.1016/j.ijheatfluidflow.2014.05.005
[6] L.H. Saw, Y. Ye, M.C. Yew, W.T. Chong, M.K. Yew, T.C. Ng, Computational fluid dynamics simulation on open cell aluminium foams for Li-ion battery cooling system, Appl. Energy 204 (2017) 1489–1499. https://doi.org/10.1016/j.apenergy.2017.04.022
[7] S. de Schampheleire, P. de Jaeger, K. de Kerpel, B. Ameel, H. Huisseune, M. de Paepe, How to study thermal applications of open-cell metal foam: experiments and computational fluid dynamics, Materials (Basel, Switzerland) 9 (2) (2016) 94. https://doi.org/10.3390/ma9020094
[8] C. Sinn, G.R. Pesch, J. Thöming, L. Kiewidt, Coupled conjugate heat transfer and heat production in open-cell ceramic foams investigated using CFD, Int. J. Heat Mass Transf. 139 (2019) 600–612. https://doi.org/10.1016/j.ijheatmasstransfer.2019.05.042
[9] A. Della Torre, F. Lucci, G. Montenegro, A. Onorati, P. Dimopoulos Eggenschwiler, E. Tronconi, G. Groppi, CFD modeling of catalytic reactions in open-cell foam substrates, Comput. Chem. Eng. 92 (2016) 55–63. https://doi.org/10.1016/j.compchemeng.2016.04.031
[10] J. von Rickenbach, F. Lucci, C. Narayanan, P. Dimopoulos Eggenschwiler, D. Poulikakos, Multi-scale modelling of mass transfer limited heterogeneous reactions in open cell foams, Int. J. Heat Mass Transf. 75 (2014) 337–346. https://doi.org/10.1016/j.ijheatmasstransfer.2014.03.060
[11] A. Aguirre, V. Chandra, E.A.J.F. Peters, J.A.M. Kuipers, M.F. Neira D'Angelo, Open-cell foams as catalysts support: a systematic analysis of the mass transfer limitations, Chem. Eng. J. 393 (2020) 124656. https://doi.org/10.1016/j.cej.2020.124656
[12] S.A. Solovev, O.V. Soloveva, I.G. Akhmetova, Y.V. Vankov, D.L. Paluku, Numerical simulation of heat and mass transfer in an open-cell foam catalyst on example of the acetylene hydrogenation reaction, ChemEngineering 6 (1) (2022) 11. https://doi.org/10.3390/chemengineering6010011
[13] Z. Nie, Y. Lin, Q. Tong, Modeling structures of open cell foams, Comput. Mater. Sci. 131 (2017) 160–169. https://doi.org/10.1016/j.commatsci.2017.01.029
[14] K. Boomsma, D. Poulikakos, Y. Ventikos, Simulations of flow through open cell metal foams using an idealized periodic cell structure, Int. J. Heat Fluid Flow 24 (6) (2003) 825–834. https://doi.org/10.1016/j.ijheatfluidflow.2003.08.002
[15] M. Bracconi, M. Ambrosetti, M. Maestri, G. Groppi, E. Tronconi, A systematic procedure for the virtual reconstruction of open-cell foams, Chem. Eng. J. 315 (2017) 608–620. https://doi.org/10.1016/j.cej.2017.01.069
[16] M. Bracconi, M. Ambrosetti, M. Maestri, G. Groppi, E. Tronconi, A fundamental investigation of gas/solid mass transfer in open-cell foams using a combined experimental and CFD approach, Chem. Eng. J. 352 (2018) 558–571. https://doi.org/10.1016/j.cej.2018.07.023
[17] M. Sadeghi, M. Mirdrikvand, G.R. Pesch, W. Dreher, J. Thöming, Full-field analysis of gas flow within open-cell foams: comparison of micro-computed tomography-based CFD simulations with experimental magnetic resonance flow mapping data, Exp. Fluids 61 (5) (2020) 1–16. https://doi.org/10.1007/s00348-020-02960-4
[18] N. Michailidis, F. Stergioudi, H. Omar, D.N. Tsipas, An image-based reconstruction of the 3D geometry of an Al open-cell foam and FEM modeling of the material response, Mech. Mater. 42 (2) (2010) 142–147. https://doi.org/10.1016/j.mechmat.2009.10.006
[19] K. Kuhlmann, C. Sinn, J.M.U. Siebert, G. Wehinger, J. Thöming, G.R. Pesch, From mCT data to CFD: an open-source workflow for engineering applications, Eng. Appl. Comput. Fluid Mech. 16 (1) (2022) 1706–1723. https://doi.org/10.1080/19942060.2022.2109758
[20] B. Manz, L.F. Gladden, P.B. Warren, Flow and dispersion in porous media: lattice-Boltzmann and NMR studies, AIChE J. 45 (9) (1999) 1845–1854. https://doi.org/https://doi.org/10.1002/aic.690450902
[21] M. Sadeghi, A. Ricke, G.R. Pesch, W. Dreher, J. Thöming, Comparative full-field velocimetry of liquid flow within monolithic catalyst carriers via CFD simulations and MRV measurements, Exp. Fluids 64 (8) (2023) 1–12. https://doi.org/10.1007/s00348-023-03681-0
[22] C. Wüstenhagen, K. John, S. Langner, M. Brede, S. Grundmann, M. Bruschewski, CFD validation using in-vitro MRI velocity data - methods for data matching and CFD error quantification, Comput. Biol. Med. 131 (2021) 104230. https://doi.org/10.1016/j.compbiomed.2021.104230
[23] M.M. Britton, MRI of chemical reactions and processes, Prog. Nucl. Magn. Reson. Spectrosc. 101 (2017) 51–70. https://doi.org/10.1016/j.pnmrs.2017.03.001
[24] J. Delannoy, C.N. Chen, R. Turner, R.L. Levin, D. Le Bihan, Noninvasive temperature imaging using diffusion MRI, Magn. Reson. Med. 19 (2) (1991) 333–339. https://doi.org/10.1002/mrm.1910190224
[25] L. Winter, E. Oberacker, K. Paul, Y. Ji, C. Oezerdem, P. Ghadjar, A. Thieme, V. Budach, P. Wust, T. Niendorf, Magnetic resonance thermometry: methodology, pitfalls and practical solutions, Int. J. Hyperth. : Off. J. Eur. Soc. Hyperthermic Oncol. N. Am. Hyperth. Group 32 (1) (2016) 63–75. https://doi.org/10.3109/02656736.2015.1108462
[26] T. Schenkel, M. Malve, M. Reik, M. Markl, B. Jung, H. Oertel, MRI-based CFD analysis of flow in a human left ventricle: methodology and application to a healthy heart, Ann. Biomed. Eng. 37 (3) (2009) 503–515. https://doi.org/10.1007/s10439-008-9627-4
[27] S. Ito, J. Jeßberger, S. Simonis, F. Bukreev, A. Kummerländer, A. Zimmermann, G. Thäter, G.R. Pesch, J. Thöming, M.J. Krause, Identification of reaction rate parameters from uncertain spatially distributed concentration data using gradient-based PDE constrained optimization, Comput. Math. Appl. 167 (2024) 249–263. https://doi.org/10.1016/j.camwa.2024.05.026
[28] D.J. Robbins, M.S. El-Bachir, L.F. Gladden, R.S. Cant, E. von Harbou, CFD modeling of single–phase flow in a packed bed with MRI validation, AIChE J. 58 (12) (2012) 3904–3915. https://doi.org/10.1002/aic.13767
[29] F. Klemens, S. Schuhmann, G. Guthausen, G. Thäter, M.J. Krause, CFD-MRI: A coupled measurement and simulation approach for accurate fluid flow characterisation and domain identification, Comput. Fluids 166 (2018) 218–224. https://doi.org/10.1016/j.compfluid.2018.02.022
[30] A. Kontogiannis, S.V. Elgersma, A.J. Sederman, M.P. Juniper, Joint reconstruction and segmentation of noisy velocity images as an inverse Navier–Stokes problem, J. Fluid Mech. 944 (2022) A40. https://doi.org/10.1017/jfm.2022.503
[31] M.J. Krause, G. Thäter, V. Heuveline, Adjoint-based fluid flow control and optimisation with lattice Boltzmann methods, Comput. Math. Appl. 65 (6) (2013) 945–960. https://doi.org/10.1016/j.camwa.2012.08.007

[32] R. Trunk, T. Weckerle, N. Hafen, G. Thäter, H. Nirschl, M.J. Krause, Revisiting the homogenized lattice Boltzmann method with applications on particulate flows, Computation 9 (2) (2021). https://doi.org/10.3390/computation9020011
[33] J.E. Marquardt, M.J. Krause, A review of the homogenized lattice boltzmann method for particulate flow simulations: from fundamentals to applications, Powders 3 (4) (2024) 500–530. https://doi.org/10.3390/powders3040027
[34] M.J. Krause, F. Klemens, T. Henn, R. Trunk, H. Nirschl, Particle flow simulations with homogenised lattice Boltzmann methods, Particuology 34 (2017) 1–13. https://doi.org/10.1016/j.partic.2016.11.001
[35] F. Klemens, B. Förster, M. Dorn, G. Thäter, M.J. Krause, Solving fluid flow domain identification problems with adjoint lattice Boltzmann methods, Comput. Math. Appl. 79 (1) (2020) 17–33. https://doi.org/10.1016/j.camwa.2018.07.010
[36] M.J. Krause, A. Kummerländer, S.J. Avis, H. Kusumaatmaja, D. Dapelo, F. Klemens, M. Gaedtke, N. Hafen, A. Mink, R. Trunk, J.E. Marquardt, M.-L. Maier, M. Haussmann, S. Simonis, OpenLB—Open source lattice Boltzmann code, Comput. Math. Appl. 81 (2021) 258–288. https://doi.org/10.1016/j.camwa.2020.04.033
[37] S. Simonis, M. Haussmann, L. Kronberg, W. Dörfler, M.J. Krause, Linear and brute force stability of orthogonal moment multiple-relaxation-time lattice Boltzmann methods applied to homogeneous isotropic turbulence, Philos. Trans. R. Soc. A 379 (2208) (2021) 20200405. https://doi.org/10.1098/rsta.2020.0405
[38] S. Simonis, S. Mishra, Computing statistical Navier–Stokes solutions, in: R. Abgrall, M. Garavello, M. Lukáčová-Medvid'ová, K. Trivisa (Eds.), Hyperbolic Balance Laws: Interplay Between Scales and Randomness, 1 in Oberwolfach Report 21, EMS Press, 2024, pp. 567–656. https://doi.org/10.4171/OWR/2024/10
[39] A. Mink, K. Schediwy, C. Posten, H. Nirschl, S. Simonis, M.J. Krause, Comprehensive computational model for coupled fluid flow, mass transfer, and light supply in tubular photobioreactors equipped with glass sponges, Energies 15 (20) (2022) 7671. https://doi.org/10.3390/en15207671
[40] S. Simonis, M. Frank, M.J. Krause, Constructing relaxation systems for lattice Boltzmann methods, Appl. Math. Lett. 137 (2023) 108484. https://doi.org/10.1016/j.aml.2022.108484
[41] A. Kummerländer, M. Dorn, M. Frank, M.J. Krause, Implicit propagation of directly addressed grids in lattice Boltzmann methods, Concurr. Comput. Pract. Exp. 35 (8) (2023) e7509. https://doi.org/10.1002/cpe.7509
[42] Ł. Łaniewski-Wołłk, J. Rokicki, Adjoint lattice Boltzmann for topology optimization on multi-GPU architecture, Comput. Math. Appl. 71 (3) (2016) 833–848. https://doi.org/10.1016/j.camwa.2015.12.043
[43] A. Kummerländer, F. Bukreev, S.F.R. Berg, M. Dorn, M.J. Krause, Advances in computational process engineering using lattice Boltzmann methods on high performance computers, in: W.E. Nagel, D.H. Kröner, M.M. Resch (Eds.), High Performance Computing in Science and Engineering '22, Springer Nature Switzerland, Cham, 2024, pp. 233–247.
[44] S. Ito, S. Großmann, F. Bukreev, J. Jeßberger, M.J. Krause, Benchmark case for the inverse determination of adsorption parameters using lattice Boltzmann methods and gradient-based optimization, Chem. Eng. Sci. 309 (2025) 121467. https://doi.org/10.1016/j.ces.2025.121467
[45] K. Yaji, T. Yamada, M. Yoshino, T. Matsumoto, K. Izui, S. Nishiwaki, Topology optimization in thermal-fluid flow using the lattice Boltzmann method, J. Comput. Phys. 307 (2016) 355–377. https://doi.org/10.1016/j.jcp.2015.12.008
[46] F. Klemens, S. Schuhmann, R. Balbierer, G. Guthausen, H. Nirschl, G. Thäter, M.J. Krause, Noise reduction of flow MRI measurements using a lattice Boltzmann based topology optimisation approach, Comput. Fluids 197 (2020) 104391. https://doi.org/10.1016/j.compfluid.2019.104391
[47] C. Geiger, C. Kanzow, Numerische Verfahren Zur Lösung Unrestringierter Optimierungsaufgaben, Springer-Verlag, 2013.
[48] R.H. Byrd, P. Lu, J. Nocedal, C. Zhu, A limited memory algorithm for bound constrained optimization, SIAM J. Sci. Comput. 16 (5) (1995) 1190–1208. https://doi.org/10.1137/0916069
[49] I. Cheylan, G. Fritz, D. Ricot, P. Sagaut, Shape optimization using the adjoint lattice Boltzmann method for aerodynamic applications, AIAA J. 57 (7) (2019) 2758–2773. https://doi.org/10.2514/1.J057955
[50] T. Fawcett, An introduction to ROC analysis, Pattern Recognit. Lett. 27 (8) (2006) 861–874. https://doi.org/10.1016/j.patrec.2005.10.010
[51] M. Levandowsky, D. Winter, Distance between sets, Nature 234 (5323) (1971) 34–35. https://doi.org/10.1038/234034a0
[52] R. Pfister, K.A. Schwarz, M. Janczyk, R. Dale, J.B. Freeman, Good things peak in pairs: a note on the bimodality coefficient, Front. Psychol. 4 (2013) 700. https://doi.org/10.3389/fpsyg.2013.00700
[53] Royal Society, Proceedings of the Royal Society of London, Taylor & Francis, 1895. URL https://books.google.de/books?id=60aL0zlT-90C.
[54] S. Simonis, N. Hafen, J. Jeßberger, D. Dapelo, G. Thäter, M.J. Krause, Homogenized lattice Boltzmann methods for fluid flow through porous media – Part I: kinetic model derivation, ESAIM: M2AN 59 (2) (2025) 789–813. https://doi.org/10.1051/m2an/2025005
[55] T. Krüger, H. Kusumaatmaja, A.V. Kuzmin, O. Shardt, G. Silva, E.M. Viggen, The lattice Boltzmann method: principles and practice, Graduate Texts in Physics, Springer and Springer International Publishing AG, [Cham], 2017.
[56] M. Sezgin, B. Sankur, Survey over image thresholding techniques and quantitative performance evaluation, J. Electron. Imaging 13 (1) (2004) 146 – 165. https://doi.org/10.1117/1.1631315
[57] M. Ángel González Ballester, A.P. Zisserman, M. Brady, Estimation of the partial volume effect in MRI, Med. Image Anal. 6 (4) (2002) 389–405. https://doi.org/10.1016/S1361-8415(02)00061-0
[58] S. Ito, A. Kummerländer, J. Jeßberger, J.L. Grafen, E. Öz, N.R. Gauger, M. Sagebaum, M.J. Krause, Generation of efficient adjoint lattice Boltzmann methods with algorithmic differentiation (2025). Available at SSRN, https://doi.org/10.2139/ssrn.6505987